

---

# Interpretable Neural ODEs for Gene Regulatory Network Discovery under Perturbations

---

Zaikang Lin<sup>\*1,2</sup> Sei Chang<sup>\*1,2</sup> Aaron Zweig<sup>1,2,3</sup> Minseo Kang<sup>1,2</sup> Elham Azizi<sup>1,3</sup> David A. Knowles<sup>1,2</sup>

## Abstract

Modern high-throughput biological datasets with thousands of perturbations provide the opportunity for large-scale discovery of causal graphs that represent the regulatory interactions between genes. Differentiable causal graphical models have been proposed to infer a gene regulatory network (GRN) from large scale interventional datasets, capturing the causal gene regulatory relationships from genetic perturbations. However, existing models are limited in their expressivity and scalability while failing to address the dynamic nature of biological processes such as cellular differentiation. We propose *PerturbODE*, a novel framework that incorporates biologically informative neural ordinary differential equations (neural ODEs) to model cell state trajectories under perturbations and derive the causal GRN from the neural ODE’s parameters. We demonstrate *PerturbODE*’s efficacy in trajectory prediction and GRN inference across simulated and real over-expression datasets.

## 1. Introduction

GRNs capture the complex regulatory interactions between genes that dictate cell function, development, and responses to environmental changes. High-throughput perturbation assays with single-cell RNA sequencing (scRNA-seq) readouts, such as Perturb-seq (Dixit et al., 2016) or open reading frame (ORF) overexpression (Joung et al., 2023), enable precise measurement of gene expression changes across cell types resulting from genetic perturbations. However, inferring GRNs from scRNA-seq experiments remains challenging due to the problem’s exponential search space.

Regression-based approaches train a separate regression for each gene from all other genes, with random forests showing particular promise (e.g., PIDC, GENIE3 and GRNBoost2). While these simple approaches have performed well in some GRN recovery benchmarks (Pratapa et al., 2020; Huynh-Thu et al., 2010; Moerman et al., 2019; Chan et al., 2017), they cannot distinguish between direct and mediated causal

effects, account for latent confounding, or generalize to unseen interventions.

In contrast, recent causal graphical models have been developed to leverage the increasing availability of perturbational datasets in single-cell genomics. Their explicit encoding of the relationships between causal variables (genes) enable them to generate samples from learned interventional distributions (Tejada-Lapuerta et al., 2023). Causal models enable tractable network inference through a continuous, albeit non-convex, optimization program that learns a directed acyclic graph (DAG) corresponding to the underlying GRN (Zheng et al., 2018; Fang et al., 2023; Brouillard et al., 2020; Lopez et al., 2022).

Causal graphical models have focused on learning structure from CRISPR based gene knockdown or overexpression based Perturb-seq. These perturbations are modest, slightly shifting cell state but not pushing cells into distinct cell types. However, new ORF overexpression single-cell experiments provide large perturbations, thereby offering insights into previously unexplored aspects of dynamic gene regulation during differentiation. In particular, the Transcription Factor (TF) Atlas applied single-cell resolution assays to systematically study the effects of overexpression of 1,836 TFs in embryonic stem cells, generating over 1.1 million cell profiles measured 7 days following TF perturbation (Joung et al., 2023). TFs, proteins that bind to the genome to regulate gene expression, play a crucial role in defining cell states. TF overexpression can induce significant changes in cell fate mimicking those of natural development, allowing us to model how TFs direct stem cells along trajectories into diverse differentiated cell types such as myocytes and neurons. Since gene regulation during differentiation is inherently dynamic, accurately capturing these dynamics is essential for effectively modeling interventional distributions under TF overexpression. Extensive florescent experiments in yeast and *E. coli* have demonstrated that gene regulatory dynamics can be effectively modeled by non-linear dynamical systems (Alon, 2006; Setty et al., 2003; Kalir & Alon, 2004).

Causal graphical models are limited in their ability to model the full complexity of high-dimensional interventional data capturing dynamic biological processes. To address these

limitations, we propose *PerturbODE*, a novel neural ODE-based framework that 1) explicitly encodes the GRN in its parameters, enabling simultaneous trajectory inference and GRN discovery, 2) maps cell states into a lower dimensional “gene module” space analogously to causal representation learning (CRL) in Schölkopf et al. (2021), 3) allows explicit input of which gene(s) were perturbed, a feature uncommon in CRL approaches, 4) can model cycles and non-linear gene interactions, and 5) leverage causal relationships to predict the effects of unseen perturbations. Trained on the TF Atlas scRNA-seq data that captures the differentiation pathways of cells perturbed by over-expression of over a thousand TFs, *PerturbODE* enables scalable and interpretable discovery of the gene dependencies that drive cellular differentiation.

## 2. Related Work

**Causal graph discovery from genetic perturbations.** Structure learning of causal graphs has recently been applied to Perturb-seq interventional experiments to infer an underlying GRN. The nodes in the encoded causal graph correspond to genes and the directed edges ideally correspond to direct causal regulatory relationships between genes. Since the number of possible DAGs grows exponentially with the number of nodes, classical causal graph discovery approaches are unable to scale beyond a modest number of genes (typically 50-200). NO-TEARS (Zheng et al., 2018) introduced a continuous optimization objective via the trace exponential acyclicity constraint, significantly simplifying the problem complexity and enabling gradient descent-based structure learning. Extensions have further improved scalability. NO-TEARS-LR (Fang et al., 2024) adds a low-rank assumption to NO-TEARS to efficiently infer large and dense DAGs. DCDI (Brouillard et al., 2020) extends the continuous optimization formulation to interventional data but can only scale up to 50 dimensions in their original implementation with the trace exponential acyclicity constraint. DCDFG (Lopez et al., 2022) addresses DCDI’s limited scalability by employing a low-rank factor graph structure and spectral radius acyclicity constraint.

**Neural ODEs for cell trajectory inference and modeling gene regulation.** Differential equation-based models have long been considered the gold-standard for modeling gene regulation due to their fidelity to our understanding of true biophysical mechanism. Neural ODEs allow flexible parameterization and efficient training with differentiable ODE integration-solvers (e.g., via the adjoint method), allowing tractable mechanistic modeling of dynamics given data Chen et al. (2018). Neural ODEs and their stochastic variants have been applied to trajectory inference, where the continuous development of cellular states is mapped over time. Jackson et al. (2023) parameterizes ODEs with recurrent neural networks (RNNs) to model dynamics be-

fore obtaining the coefficient of partial determination to represent the contribution of each TF. (Hossain et al., 2024) incorporates kinetics using biological priors (e.g., using the Hill function) and explicitly encodes the GRN as model parameters, but requires densely sampled data points along a pseudotime trajectory. However, both methods are designed to learn from a single experimental environment and cannot leverage information from multiple interventions.

**Causal graph learning through stationary diffusion.** The recently proposed method Bicycle (Rohbeck et al., 2024) considers the GRN as the linear drift of a stable Ornstein-Uhlenbeck (OU) process, approximating the steady state distribution under each intervention induced by the OU process by solving the Lyapunov equation. Despite the novelty in methodology, Bicycle can only handle a hundred or so genes.

**Key Limitations.** Despite recent improvements to network inference, causal graphical methods remain difficult to scale and lack the expressivity to model cellular dynamics and regulatory cycles. Existing neural ODE-based methods (Hossain et al. (2024) and Jackson et al. (2023)) learn GRNs from a single experimental environment and cannot handle multiple genetic perturbations. *PerturbODE* combines causal structure learning and trajectory inference into a realistic and scalable framework that accurately captures cellular dynamics and infers the underlying GRN from thousands of perturbations.

## 3. Methods

Let  $\mathcal{I} = \{I_0, I_1, \dots, I_K\}$  represent a set of  $K + 1$  intervention regimes, with  $I_0$  denoting the control regime (no intervention). The training dataset  $\mathcal{D} = \{Y^{(r)}\}_{r=0}^K$  is a family of empirical distributions in the gene expression space, each corresponding to an intervention regime.  $Y^{(r)} \in \mathbb{R}^{n_r \times d}$  represents the  $d$ -dimensional gene expression measurements for  $n_r$  cells under intervention regime  $I_r$ .  $Y^{(0)}$ , the gene expression under the control regime, is used as the unperturbed initial state from which we integrate our neural ODE function  $f_r$  to predict the perturbation effect and final gene expression state under a given intervention.

### 3.1. Neural ODE formulation for over-expression with shift intervention

For any cell subject under intervention  $I_r \in \mathcal{I} \setminus \{I_0\}$ , its cellular dynamics are described by the ODE,

$$\frac{\partial y^{(r)}(t)}{\partial t} = f_r(y^{(r)}(t)) = A\sigma(\alpha \circ (By^{(r)}(t) - \beta)) + \sum_{j \in I_r} s_j \cdot \delta_j - Wy^{(r)}(t), \quad (1)$$

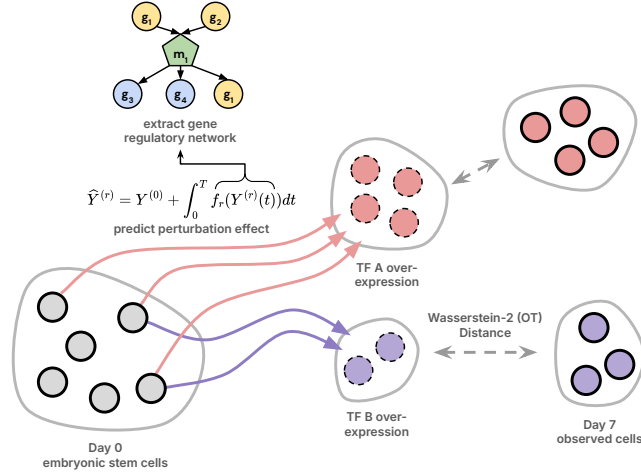


Figure 1. PerturbODE models the effect of a TF perturbation on stem cell differentiation by integrating the learned neural ODE function  $f$  from the initial distribution of stem cell gene expression  $Y^{(0)}$  under intervention  $r$ . The predicted gene expression values  $\hat{Y}^{(r)}$  are then compared to the observed differentiated expression values using the Wasserstein distance. From the parameters of  $f$ , we extract an underlying GRN that represents the regulatory relationships through gene modules.

where  $y^{(r)}(t) \in \mathbb{R}^d$  represents the expression vector at time  $t$  for a cell under intervention  $I_r$ .

This system encapsulates the interaction between genes through a Multi-Layer Perceptron (MLP) with a single hidden layer. Each neuron in the hidden layer is analogous to a gene module encapsulating co-regulated genes or biological pathways as outlined in Segal et al. (2005). Module-based regulatory network structures have been established in prior literature. A well-characterized example is the regulatory circuit of E. coli’s flagella production (Macnab, 2003; Alon, 2006). In Appendix A.12, we illustrate how this structure could be represented as a two-layer MLP.

The matrix  $B \in \mathbb{R}^{l \times d}$  represents a linear transformation from the  $d$ -dimensional gene expression  $Y^{(r)}(t)$  to a  $l$ -dimensional latent (“module”) space.  $B_{jm}$  is the signed effect of  $j$ -th gene’s expression on the  $m$ -th module.

The gene module signals are then non-linearly transformed after shift and scaling through the non-linear activation function  $\sigma(\cdot) : \mathbb{R}^l \rightarrow \mathbb{R}^l$ . We use the logistic sigmoid function for gene module activation  $\sigma(\cdot)$  due to its equivalence (when modeling log expression) to the Hill function, which, following basic chemistry principles, represents the effect of TF concentration on target gene transcription rate (Alon, 2006). The vector  $\beta \in \mathbb{R}^l$  is a strictly positive bias that shifts the activation threshold of the function  $\sigma$  in each module. The vector  $\alpha \in \mathbb{R}^l$  is a scaling factor that modulates the rate of activation through a Hadamard (i.e., elementwise) product ( $\circ$ ) with the gene modules.

The module activations regulate downstream genes by combining linearly with those from other modules. The matrix

$A \in \mathbb{R}^{d \times l}$  maps the  $l$ -dimensional latent vector back to the  $d$ -dimensional gene expression space.  $A_{mj}$  represents the influence of the  $m$ -th module on the transcription rate of the  $j$ -th gene.

The interaction between genes mediated by modules encodes our estimate of the GRN matrix,  $\mathbf{G} = A \text{diag}(\alpha)B$ . Conveniently, working with the lower-dimensional module space reduces our task from learning the full gene-to-gene matrix of size  $d \times d$  (i.e.,  $d^2$  parameters) to learning two factorized graphs of size  $d \times l$  (i.e.  $2dl$  parameters).

The matrix  $W \in \mathbb{R}^{d \times d}$  is diagonal with strictly positive entries, such that  $W_{ii} > 0$  is the decay rate for gene  $i$ . The decay component  $-Wy^{(r)}(t)$  represents cellular RNA levels decreasing over time due to molecular decay and concentration dilution as the cells grow and divide. Decay not only accurately models the regulatory biology but also encourages stability in the ODE system to prevent extreme levels of gene expression by creating a trapping region.

Interventions on the system are captured by shift term  $\delta_j = \mathbf{e}_j \in \mathbb{R}^d$ , a standard basis vector corresponding to the induced over-expression of gene  $j$  (which in our case is a TF). The vector  $\mathbf{e}_j$  encodes a 1 in the  $j^{\text{th}}$  entry and 0 in all other entries, enabling variable dynamics between cells with over-expression of different TFs. Scaling term  $s = (s_1, s_2, \dots, s_d)^\top$  specifies the strength of each intervention on each gene. Importantly, each entry in  $s$  is unique to a given intervention, while all other learned model parameters ( $A, B, W, \alpha$ , and  $\beta$ ) are shared across all interventions.

### 3.2. Neural ODE formulation with perfect intervention

We adapt PerturbODE to model perfect interventions. Gene knockout or over-expression (CRISPR-a) under perfect intervention is modeled by removing the intervened genes' dependencies on parent nodes. In a system subject to a set  $I_r$  of perfect interventions, the corresponding ODE is,

$$\begin{aligned} \frac{\partial y^{(r)}}{\partial t} &= M_r A \sigma(\alpha \circ (B y^{(r)}(t) - \beta)) \\ &+ \sum_{j \in I_i} s_j \cdot \delta_j - W y^{(r)}(t) \end{aligned} \quad (2)$$

where  $M_r = \mathbf{I} - \sum_{j \in I_r} \text{diag}(\delta_j)$  is a masking matrix that removes the effect of other genes on the perturbed gene(s). For over-expression,  $s_j > 0$  for all  $j$ , whereas for knockout we set  $s_j = 0$  for all  $j$ .

### 3.3. Mapping dynamics to targets using optimal transport

We train  $f_r$  so that cells from  $Y^{(0)}$  pushed forward through the dynamics fall close to  $Y^{(r)}$ . Specifically, we compute our target predictions  $\hat{Y}^{(r)}$  by numerically solving the ODE integration for each cell in the initial distribution,

$$\begin{aligned} \hat{Y}^{(r)} &= [\phi_T^r(y_1^{(0)}), \dots, \phi_T^r(y_{n_r}^{(0)})]^\top \\ \phi_T^r(y_j^{(0)}) &= y_j^{(0)} + \int_0^T f_r(y_j^{(r)}(t)) dt \end{aligned} \quad (3)$$

where  $j$  indexes cells in  $Y^{(0)}$  and  $\phi_T^r$  is the flow map of the ODE under intervention  $I_r$  mapping initial cell state  $y_j^{(0)}$  to its position at time  $T$ .

Given the lack of one-to-one correspondence between cells in the initial distribution  $Y^{(0)}$  and the samples in the target distributions, we assess the quality of our predictions by measuring the Wasserstein-2 distance between observed distribution  $Y^{(r)}$  and predicted distribution  $\hat{Y}^{(r)}$ ,

$$W_2(X, \hat{X}) = \left( \min_{\Gamma \sim \Pi(X, \hat{X})} \sum_{x,y} \|X_x - \hat{X}_y\|_2^2 \Gamma_{xy} \right)^{1/2}, \quad (4)$$

where  $\Pi$  represents the set of all optimal transport plans between each sample from data distributions  $X$  and  $\hat{X}$ , and  $\Gamma$  represents the minimal-cost transport plan used to measure the dissimilarity between  $X$  and  $\hat{X}$ . The total loss function is defined as the average  $W_2$  between  $\hat{Y}^{(r)}$  and  $Y^{(r)}$  for all perturbations in  $\mathcal{I}$  in addition to the  $L_1$  norm of  $B$  to encourage sparsity,

$$\mathcal{L}(\theta) = W_2(Y^{(r)}, \hat{Y}^{(r)}) + \lambda |B|_1. \quad (5)$$

During training, for each intervention  $I_r$ , we push the control samples  $Y^{(0)}$  through the map  $\phi_T^r$  to obtain the predicted targets  $\hat{Y}^{(r)}$ . We backpropagate through the loss

and ODE solver to obtain gradients for all parameters.  $L_1$  penalty is enforced only on  $B$  because the network motif of a multiple-input feed-forward loop is significantly less common than that of a multiple-output feed-forward loop in known GRNs of yeast and E. coli (Kashtan et al., 2004).

During each epoch, PerturbODE iterates through all intervention regimes in  $\mathcal{I}$ . Further details on data splitting and loss convergence can be found in Appendix A.8.

### 3.4. Diffusion-based regularization of neural dynamics

PerturbODE can optionally augment the primary training objective by using diffused target samples as alternative initial states. This additional regularization encodes our prior expectation that the final cell states should be locally stable, helping to form a local contraction map that implies a locally stable fixed point, as ensured by the Contraction Mapping Theorem (Hunter & Nachtergaele, 2000). Interestingly, the stable fixed points establish the theoretical equivalence between PerturbODE and a deterministic structural causal model (SCM) (Mooij et al., 2013; Schölkopf et al., 2021).

The augmentation involves diffusing  $Y^{(r)}$  using Brownian motion with a time step  $\Delta t$  to generate diffused targets  $Y_{\text{diff}}^{(r)}$ . Across a reduced time span  $t \leq T$ ,  $Y_{\text{diff}}^{(r)}$  is pushed forward through  $\phi_t^{(r)}$  to obtain the predicted targets  $\hat{Y}_{\text{diff}}^{(r)}$ , and we backpropagate against the augmented loss  $\hat{\mathcal{L}} = W_2(\hat{Y}_{\text{diff}}^{(r)}, Y^{(r)}) + \lambda |B|_1$ . During training, we alternate between using control samples  $Y^{(0)}$  and diffused targets  $Y_{\text{diff}}^{(r)}$  for each intervention. Information on the diffusion training hyperparameters can be found in Appendix A.2.2.

## 4. Results

We compare PerturbODE to the causal graph discovery methods DCDFG (Lopez et al., 2022), DCDI (Brouillard et al., 2020), NO-TEARS (Zheng et al., 2018), NO-TEARS-LR (Fang et al., 2023), and Bicycle (Rohbeck et al., 2024) through extensive experiments on both simulated and large-scale perturbational scRNA-seq datasets. These methods are most appropriate for comparison as they are equipped to learn a causal GRN from multiple interventions without requiring multiple time points or pseudotime.

PerturbODE and Bicycle can distinguish positive and negative edges, whereas DCDI and DCDFG only identify edge existence. When evaluating PerturbODE and Bicycle, we treat incorrect sign as a false positive. Hence, in simulated data, we used ground truth networks that contain only positive edges. For the TF Atlas, the literature-curated GRN edges consist only of positive edges.

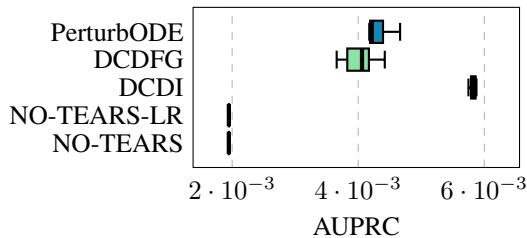
#### 4.1. GRN inference on SERGIO simulated datasets

SERGIO (Dibaenia & Sinha, 2020) simulates single-cell gene expression data by modeling regulation of each gene by multiple TFs according to a user-provided ground-truth GRN. SERGIO can simulate mature cells of any cell type in steady state or stem cells differentiating to multiple fates. Cells are initialized at the mean of the steady state distribution and then pushed through a stochastic differential equation (SDE) parameterized by the provided GRN.

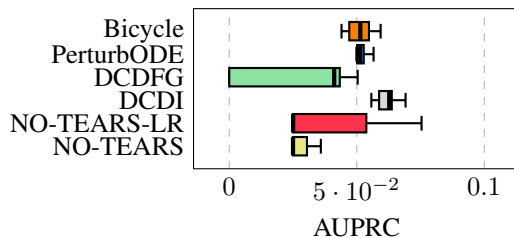
We extend SERGIO to simulate gene expression with over-expression perturbations. We implement interventions by masking the transcription induced by TF interactions (analogously to  $M_r$  in Equation 2) of the intervened genes and adding a scalar to the intervened gene’s transcription rate. We select an experimentally curated GRN identified for yeast cells with dimension 400 as the input to SERGIO for simulation (Liu et al., 2015). The output synthetic dataset from SERGIO consists of 10,100 cells generated from 100 intervention schemes each targeting 5 genes and one non-intervention (control) scheme. Each regime contains measurements of 100 cells. (Details specification for SERGIO simulator can be found in Appendix A.11.) To evaluate the models against a diverse range of networks, we simulate ten random DAGs with dimension 100 in the same manner. For comparison, we evaluate the models’ performance using the area under the precision-recall curve (AUPRC). Other metrics exhibited strong sensitivity to user-selected threshold values for edge classification, making them unreliable for benchmarking. Further details on the effects of thresholding and varying the number of modules are presented in Appendix A.5 and A.5.2.

Performances across models in data simulated with a known yeast GRN (400 genes) are compared in Figure 2a. In this setting, Bicycle could not be evaluated due to the method’s inability to scale to 400 genes. While PerturbODE does not outperform DCDI, it outperforms DCDFG, NO-TEARS, and NO-TEARS-LR. PerturbODE’s performance advantage becomes more apparent when the number of causal variables increase substantially, as DCDI fails to scale at higher data dimensions.

For data simulated with 10 random GRNs (100 genes), PerturbODE and Bicycle yield similar performance, while DCDI outperforms them marginally (Figure 2b). DCDFG performs marginally worse than PerturbODE and Bicycle, and NO-TEARS and NO-TEARS-LR perform significantly worse.



(a) Known yeast GRN (400 genes)



(b) 10 random acyclic GRNs (100 genes)

Figure 2. Performance metrics on SERGIO-simulated data assuming perfect intervention over-expression (CRISPR-a).

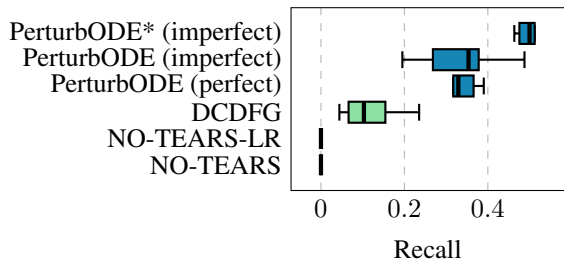
#### 4.2. GRN inference on the TF Atlas

We trained PerturbODE on the TF Atlas to evaluate its performance on a large-scale real dataset. The TF Atlas overexpresses TFs and uses scRNA-seq to measure cell states after 7 days of perturbation (Joung et al., 2023). As this dataset maps the interventional effects of TF overexpression, PerturbODE’s inferred GRNs can uncover TF-to-TF interactions and higher-level network structure through TF modules.

We used the control samples (mCherry) as the initial gene expression state for solving the neural ODE (Eq. 1), while the final gene expression states correspond to cells after 7 days of TF overexpression. We evaluate the model’s performance using three well-studied and experimentally validated human GRNs derived from extensive RNA-seq and ATAC-seq measurements (see Appendix A.9 for further details). Notably, the ground truth GRNs only contain positive directed edges, restricting our evaluation to true positives and false negatives for benchmarking GRN edge detection. Consequently, we compute a  $p$ -value via a statistical significance test comparing the inferred GRN to random matrices and the recall based on edge prediction across all three GRNs. Details on thresholding and comparison to random matrices can be found in Appendix A.2.1 and A.3.

We compare to DCDFG, NO-TEARS, and NO-TEARS-LR by training on the union of the top 500 highly variable genes and experimentally intervened genes that are differentially expressed (817 genes in total). Bicycle and DCDI cannot handle datasets of this scale, making them unsuitable for comparison. PerturbODE’s GRN estimation under both per-

perfect and imperfect intervention models are evaluated. PerturbODE significantly outperforms DCDFG, NO-TEARS, and NO-TEARS-LR in recall with more significant  $p$ -values (Fig. 3). PerturbODE\* denotes the version with tunable over-expression strength  $s$  for each gene. PerturbODE\* with imperfect intervention is the best performing model in terms of recall scores and  $p$ -values in this dataset.



(a) Recall

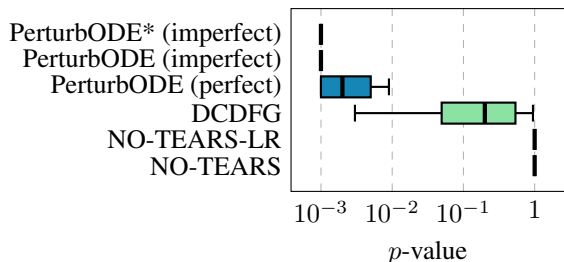
(b)  $p$ -value

Figure 3. GRN inference performance on TF Atlas dataset (817 genes). Models with different numbers of modules are compared.

Since our ground truth network only consists of known edges, we plot the recall across models at different sparsity levels by varying the thresholds for edge classification (Fig. 4). PerturbODE\* with imperfect intervention outperforms all other methods at almost all sparsity levels.

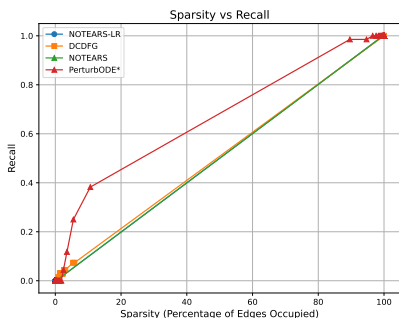


Figure 4. Recall across models on TF Atlas at various sparsity levels.

**Prediction of held-out interventions** Predicting the effects of unseen, i.e., heldout, interventions is a particularly challenging task. Here we randomly select ten overexpressed TFs to be held out simultaneously during training. Note that their expression levels of these genes are observed, but their perturbations are not trained on. For this task, we only compare PerturbODE with linear SCMs (NO-TEARS and NO-TEARS-LR). DCDFG cannot sample cells given a learned GRN, and DCDI does not scale to this data. For the linear SCMs, over-expression is implemented as imperfect shift intervention by adding a bias to the mean of the distribution modeling the intervened nodes (for details, see Appendix A.4).

We evaluate the predictive performance through Pearson correlation,  $W_2$  distance between the predicted and true distributions, and manual inspection via low dimensional (UMAP) embeddings. Pearson correlation is computed between the average predicted gene expression and the average gene expression of experimentally perturbed cells, while  $W_2$  distance is calculated between the full distributions of predicted and observed gene expressions.

Table 1. Predictive performance on 10 held-out interventions in TF-Atlas.

Method	$W_2$	Pearson ( $r$ )
NO-TEARS	$396 \pm 232$	$-0.03 \pm 0.02$
NO-TEARS-LR	$105 \pm 1$	$0.03 \pm 0.01$
<b>PerturbODE</b>	<b><math>84 \pm 183</math></b>	<b><math>0.67 \pm 0.14</math></b>

Table 2. Test errors ( $W_2$ ) for TF over-expressions across different models.

TF Over-expression	<b>PerturbODE</b>	NO-TEARS-LR	NO-TEARS
ZNF69	<b>85.38</b>	106.02	164.88
SETDB1	261.94	<b>97.19</b>	157.86
POU2AF1	300.81	<b>105.49</b>	163.09
ZBTB37	<b>69.44</b>	107.12	165.93
IRF3	<b>73.64</b>	111.17	170.13
ID1	<b>79.64</b>	109.71	168.66
TEAD1	244.55	<b>106.08</b>	163.45
ASCL1	<b>94.08</b>	134.77	192.73
KCNIP4	<b>82.66</b>	104.72	163.74
MSX2	<b>66.69</b>	103.69	164.63

PerturbODE significantly outperforms the other methods in terms of Pearson correlation and  $W_2$  distance with the held-out interventions (Table 1 and Table 2). For vast majority of the held-out perturbations, PerturbODE makes considerably better predictions. For additional context on the scale of  $W_2$ , before model training, the predicted target distributions have an average  $W_2$  distance of over 2000 from the ground truth distributions. When we visualize our predictions compared to the linear SCMs across held-out TFs through UMAP, we show that PerturbODE’s predictions are much closer to the observed distributions (Figure 5 and Appendix A.7.1).

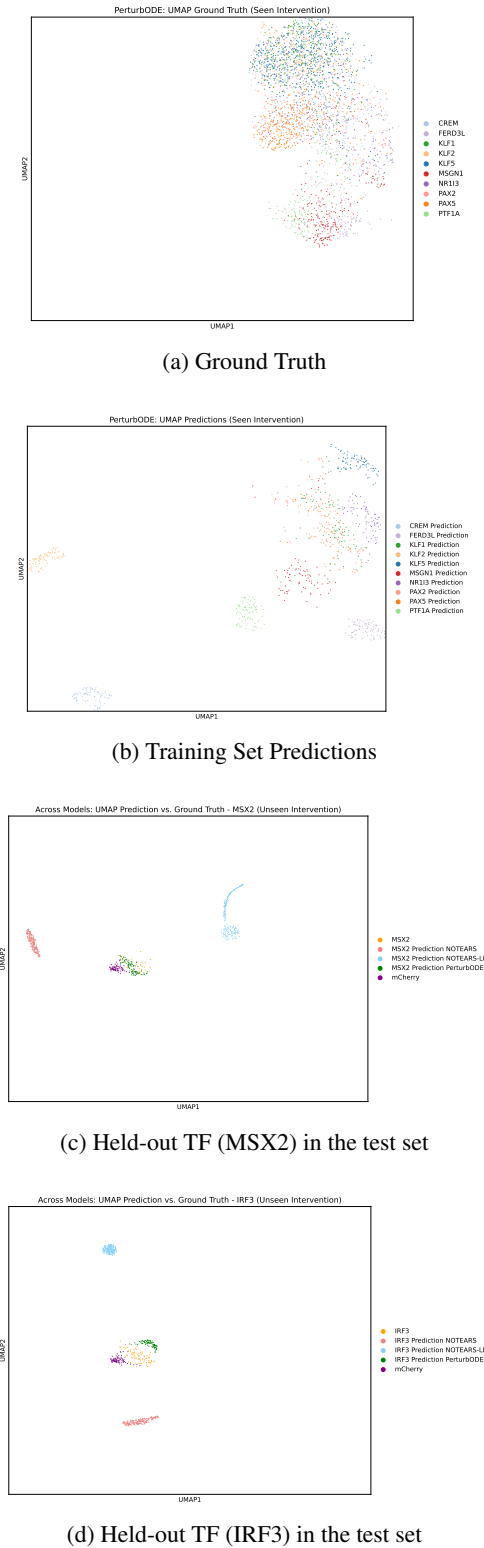


Figure 5. Visualization of the cell embeddings for the trajectory predictions of 10 transcription factors (TFs) in the training set and two held-out TFs — MSX2 and IRF3 — in the test set using UMAP1 and UMAP2. Each point represents a cell’s embedding in the reduced-dimensional space.

#### 4.2.1. ANALYSIS OF INFERRED GENE MODULES

PerturbODE’s framework enables direct interpretation of the inferred gene modules, which encapsulate multiple gene to gene interactions. These interactions are extracted from the  $A$  and  $B$  matrices (Eq. 1), where the entries in  $B$  represent directed edges from upstream genes to gene modules, and the entries in  $A$  map the modules to downstream genes.

To highlight the advantages of PerturbODE’s interpretability, we analyze the 200 inferred latent gene modules obtained from training on the TF Atlas dataset. We computed a test score based on the number of correct gene regulators and targets in the GRN selected by each module (Section A.3). We visualize seven modules with the highest scores in Fig. 20, each corresponding to directed edges found in experimentally validated GRNs (Appendix A.9). The modules in (a) - (e) encapsulate the GRN responsible for specification of the anterior-posterior axis in development (Neijts et al., 2017). (f) and (g) successfully capture known GRNs responsible for inducing trophoblasts and vascular endothelial cells respectively (Krendl et al., 2017; Dejana et al., 2007). Additionally, we compared the inferred modules to Erdős-Rényi random matrices in terms of the number of correct regulators and targets selected, yielding  $p$ -values of less than 0.001 (Appendix A.3). Significant  $p$ -values indicate that the correct genes are not assigned to the modules by random chance. By inspecting the modules, we demonstrate that PerturbODE recovers the appropriate gene network structure, clustering genes from the same GRN and accurately inferring edges between them.

Gene Enrichment Analysis of Selected Modules - Clustered Heatmap

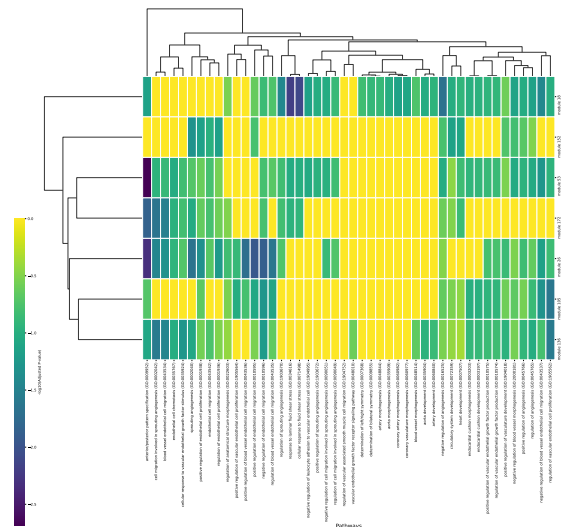


Figure 6. Gene enrichment clustered heatmap (average linkage) for selected modules.

We further validate PerturbODE’s inferred gene modules

through gene set enrichment analysis (GSEA), which evaluates the overlap between genes associated with known biological pathways and genes within each predicted module. Figure 6 presents a clustered heatmap of statistically significant pathway enrichments across modules (a) to (g), with details provided in Appendix A.14. Our analysis reveals biologically coherent patterns that align with cellular differentiation. Modules 172 and 136 show enrichment in pathways specific to vascular endothelial cells. Meanwhile, modules 26, 172, 136, 18, and 53 demonstrate strong enrichment in anterior-posterior (A-P) axis specification, with module 53 showing the strongest significance. Additionally, module 18 exhibits significant enrichment in pathways related to angiogenesis and fluid stress response.

## 5. Discussion

The question of identifiability of the ODE parameters is somewhat delicate. We assume the true underlying dynamics to be a deterministic system, inducing a family of stable fixed points, each corresponding to a perturbation. Authors (2025) has proved identifiability in a low noise regime for an SDE extension of our model. It in principle follows for the noiseless ODE case that the parameters are identifiable (up to permutations) when the number of interventions exceeds the gene dimension. Future work could explore a rigorous proof for this case.

## 6. Conclusion

PerturbODE is a highly scalable and biologically-grounded causal approach to inferring GRNs from high-throughput genetic perturbation data. Building on the success of dynamical systems in modeling gene regulation and single-cell trajectories, our method presents a compelling alternative to traditional SCMs for causal discovery. At its core, PerturbODE employs a two-layer neural network with sigmoid activation that mirrors cellular regulatory processes. The framework achieves both strong predictive performance and biological interpretability of the learned parameters. In benchmarks, PerturbODE outperforms existing scalable methods on SERGIO-simulated datasets and large-scale single-cell experiments, while performing competitively against state-of-the-art but less scalable methods like DCDI. Notably, PerturbODE can accurately predict cellular responses to previously unseen perturbations. Future work will incorporate ATAC-seq and ChIP-seq data to narrow down the candidate regulatory targets and mitigate false discoveries. Furthermore, training PerturbODE on scRNA-seq datasets with multiple time points will help the model better distinguish direct and indirect causal effects between genes (Davidson, 2006, p.133-134).

## Impact Statement

This paper presents work whose goal is to advance the application of Machine Learning to genomics. There are many potential societal consequences of our work, none which we feel must be specifically highlighted here.

## References

- Alon, U. *An Introduction to Systems Biology: Design Principles of Biological Circuits*. CRC Press Taylor & Francis Group, A Chapman & Hall Book, 2006.
- Authors, A. Towards identifiability of interventional stochastic differential equations. 2025.
- Brouillard, P., Lachapelle, S., Lacoste, A., Lacoste-Julien, S., and Drouin, A. Differentiable causal discovery from interventional data. In *Proceedings of the 34th Conference on Neural Information Processing Systems (NeurIPS 2020)*, Vancouver, Canada, 2020.
- Chan, T. E., Stumpf, M. P. H., and Babbie, A. C. Gene regulatory network inference from single-cell data using multivariate information measures. *Cell Systems*, 5(3): 251–267.e3, September 2017. doi: 10.1016/j.cels.2017.08.014.
- Chen, R. T. Q. torchdiffEq, June 2021. URL <https://github.com/rtqichen/torchdiffEq>.
- Chen, R. T. Q., Rubanova, Y., Bettencourt, J., and Duvenaud, D. K. Neural ordinary differential equations. In *Advances in Neural Information Processing Systems 31 (NeurIPS 2018)*, pp. 6571–6583, 2018.
- Davidson, E. H. *The Regulatory Genome: Gene Regulatory Networks in Development and Evolution*. Academic Press, 2006. doi: 10.1016/B978-0-12-088563-3.X5018-4.
- Dejana, E., Taddei, A., and Randi, A. Foxs and ets in the transcriptional regulation of endothelial cell differentiation and angiogenesis. *Biochim. Biophys. Acta*, 1775:298–312, 2007. doi: 10.1016/j.bbcan.2007.05.003. URL <https://doi.org/10.1016/j.bbcan.2007.05.003>.
- Dibaenia, P. and Sinha, S. Sergio: A single-cell expression simulator guided by gene regulatory networks. *Cell Systems*, 11(3):252–271.e11, 2020. ISSN 2405-4712. doi: <https://doi.org/10.1016/j.cels.2020.08.003>. URL <https://www.sciencedirect.com/science/article/pii/S2405471220302878>.
- Dixit, A., Parnas, O., Li, B., Chen, J., Fulco, C. P., Jerby-Aron, L., Marjanovic, N. D., Dionne, D., Burks, T., Raychowdhury, R., Adamson, B., Norman, T. M., Lander, E. S., Weissman, J. S., Friedman, N., and

- Regev, A. Perturb-seq: Dissecting molecular circuits with scalable single-cell RNA profiling of pooled genetic screens. *Cell*, 167(7):1853–1866.e17, December 2016. URL <https://pmc.ncbi.nlm.nih.gov/articles/PMC5181115/>.
- E, W., Li, T., and Vanden-Eijnden, E. *Applied Stochastic Analysis*, volume 199 of *Graduate Studies in Mathematics*. American Mathematical Society, 2019.
- Fang, Z., Zhu, S., Zhang, J., Liu, Y., Chen, Z., and He, Y. On low rank directed acyclic graphs and causal structure learning. *arXiv preprint arXiv:2006.05691*, cs.LG, 2023. <https://arxiv.org/abs/2006.05691v2>.
- Fang, Z., Zhu, S., Zhang, J., Liu, Y., Chen, Z., and He, Y. On low-rank directed acyclic graphs and causal structure learning. *IEEE Transactions on Neural Networks and Learning Systems*, 35(4):4924–4937, 2024. doi: 10.1109/TNNLS.2023.3273353.
- Feydy, J., S ejourn e, T., Vialard, F.-X., Amari, S.-i., Trounev, A., and Peyr e, G. Interpolating between optimal transport and mmd using sinkhorn divergences. In *The 22nd International Conference on Artificial Intelligence and Statistics*, pp. 2681–2690, 2019.
- Gorin, G. and Pachter, L. Length biases in single-cell rna sequencing of pre-mrna. *Biophysical Reports*, 3(1):100097, 2023. doi: 10.1016/j.bpr.2022.100097. URL <https://doi.org/10.1016/j.bpr.2022.100097>.
- Hossain, I., Fanfani, V., Fischer, J., Quackenbush, J., and Burkholz, R. Biologically informed neuralodes for genome-wide regulatory dynamics. *Preprint*, 2024. Available at [source if applicable].
- Hunter, J. K. and Nachtergaele, B. *Applied Analysis*. University of California at Davis, Department of Mathematics, University of California at Davis, 2000.
- Huynh-Thu, V. A., Irrthum, A., Wehenkel, L., and Geurts, P. Inferring regulatory networks from expression data using tree-based methods. *PLoS ONE*, 5(9):e12776, 2010. doi: 10.1371/journal.pone.0012776.
- Jackson, C. A., Beheler-Amass, M., Tj arnberg, A., Suresh, I., mei Hickey, A. S., Bonneau, R., and Gresham, D. Simultaneous estimation of gene regulatory network structure and rna kinetics from single cell gene expression. *bioRxiv*, 2023. doi: 10.1101/2023.09.21.558277. URL <https://doi.org/10.1101/2023.09.21.558277>.
- Joung, J., Ma, S., Tay, T., Geiger-Schuller, K. R., Kirchgatterer, P. C., Verdine, V. K., Guo, B., Arias-Garcia, M. A., Allen, W. E., Singh, A., Kuksenko, O., Abudayyeh, O. O., Gootenberg, J. S., Fu, Z., Macrae, R. K., Buenrostro, J. D., Regev, A., and Zhang, F. A transcription factor atlas of directed differentiation. *Cell*, 186:209–229, 2023. doi: 10.1016/j.cell.2022.11.026. URL <https://doi.org/10.1016/j.cell.2022.11.026>.
- Kalir, S. and Alon, U. Using a quantitative blueprint to reprogram the dynamics of the flagella gene network. *Cell*, 117(6):713–720, 2004. doi: 10.1016/j.cell.2004.05.010.
- Kashtan, N., Itzkovitz, S., Milo, R., and Alon, U. Topological generalizations of network motifs. *Physical Review E*, 70(3):031909, 2004. doi: 10.1103/PhysRevE.70.031909.
- Krendl, C., Shaposhnikov, D., Rishko, V., Ori, C., Ziegenhain, C., Sass, S., Simon, L., M uller, N., Straub, T., Brooks, K., et al. Gata2/3-tfap2a/c transcription factor network couples human pluripotent stem cell differentiation to trophectoderm with repression of pluripotency. *Proc. Natl. Acad. Sci. USA*, 114:E9579–E9588, 2017. doi: 10.1073/pnas.1708341114. URL <https://doi.org/10.1073/pnas.1708341114>.
- Liu, Z.-P., Wu, C., Miao, H., and Wu, H. Regnetwork: an integrated database of transcriptional and post-transcriptional regulatory networks in human and mouse. *Database*, 2015:bav095, 2015. doi: 10.1093/database/bav095. URL <http://www.regnetworkweb.org>.
- Lopez, R. Dcdfig: Large-scale differentiable causal discovery of factor graphs. <https://github.com/Genentech/dcdfig>, 2024. Accessed: 2024-09-19.
- Lopez, R., H utter, J.-C., Pritchard, J. K., and Regev, A. Large-scale differentiable causal discovery of factor graphs. *36th Conference on Neural Information Processing Systems (NeurIPS 2022)*, October 2022.
- Macnab, R. M. How bacteria assemble flagella. *Annual Review of Microbiology*, 57:77–100, 2003. doi: 10.1146/annurev.micro.57.030502.090832. First published online as a Review in Advance on May 1, 2003.
- Moerman, T., Santos, S. A., Gonz alez-Blas, C. B., Simm, J., Moreau, Y., Aerts, J., and Aerts, S. Grnboost2 and arboreto: Efficient and scalable inference of gene regulatory networks. *Bioinformatics*, 35(12):2159–2161, 2019. doi: 10.1093/bioinformatics/bty916. URL <https://academic.oup.com/bioinformatics/article/35/12/2159/5184284>.
- Mooij, J. M., Janzing, D., and Sch olkopf, B. From ordinary differential equations to structural causal models: The deterministic case. *arXiv preprint arXiv:1312.4180*, 2013.

- Neijts, R., Amin, S., van Rooijen, C., and Deschamps, J. Cdx is crucial for the timing mechanism driving colinear hox activation and defines a trunk segment in the hox cluster topology. *Developmental Biology*, 422(2):146–154, 2017.
- Pratapa, A., Jalihal, A. P., Law, J. N., Bharadwaj, A., and Murali, T. M. Benchmarking algorithms for gene regulatory network inference from single-cell transcriptomic data. *Nature Methods*, 17:147–154, 2020. doi: 10.1038/s41592-019-0690-6. URL <https://doi.org/10.1038/s41592-019-0690-6>.
- Rohbeck, M., Clarke, B., Mikulik, K., Pettet, A., Stegle, O., and Ueltzhöffer, K. Bicycle: Intervention-based causal discovery with cycles. In *Proceedings of Machine Learning Research*, volume 236, pp. 209–242. 3rd Conference on Causal Learning and Reasoning, 2024.
- Schölkopf, B., Locatello, F., Bauer, S., Ke, N. R., Kalchbrenner, N., Goyal, A., and Bengio, Y. Towards causal representation learning. *arXiv preprint arXiv:2102.11107*, 2021.
- Segal, E., Pe’er, D., Regev, A., Koller, D., and Friedman, N. Learning module networks. *Journal of Machine Learning Research*, 6:557–588, 2005.
- Setty, Y., Mayo, A., Surette, M., and Alon, U. Detailed map of a cis-regulatory input function. *Proceedings of the National Academy of Sciences*, 100(13):7702–7707, 2003.
- Tejada-Lapuerta, A., Bertin, P., Bauer, S., Aliee, H., Bengio, Y., and Theis, F. J. Causal machine learning for single-cell genomics. *Cell Systems*, 2023. doi: 10.1016/j.cels.2023.08.014. URL <https://doi.org/10.1016/j.cels.2023.08.014>.
- Zheng, X., Aragam, B., Ravikumar, P., and Xing, E. P. Dags with no tears: Continuous optimization for structure learning. *Carnegie Mellon University*, November 2018. Available online at <https://github.com/xunzheng/notears>.

## A. Appendix

### A.1. Preprocessing

The scRNA-seq gene expression matrix is normalized per cell by  $10^4$  and  $\log(1 + X)$  transformed. The total gene expression vector comprises RNA counts for  $N$  genes consisting of all the TF over-expression genes  $j$  and the top  $k = 817$  variable genes.

For each TF gene  $j$ , we perform a Mann-Whitney U test on differential gene expression of TF  $j$  between the unperturbed control samples in  $X_0$  and over-expressed samples in  $X_j$  consisting of  $n_j$  cells. The returned p-value  $p_j$  from the U test determines whether over-expression of the targeted TF gene  $j$  is sufficiently induced in the experiments. The dataset is then filtered based on the criteria  $\mathcal{D} = \{X_j \mid p_j < 0.1 \text{ and } n_j \geq 10, \forall j \in \{1, 2, \dots, M\}\}$ .

Over-expression distributions of the genes encoding the GRNs of interest are added to the training and validation dataset. In addition, when training for GRN inference only without trajectory prediction, distributions of TF over-expression encoded by the marker genes of the cell types or the developmental role targeted by the genes in the GRNs are included in the joint train, test, and validation dataset.

We design a train-test split based on TF over-expression genes to select  $\mathcal{D}_{\text{train, val}}$  and  $\mathcal{D}_{\text{test}}$ . For each  $X_j \in \mathcal{D}_{\text{train, val}}$  where  $n_j \geq 100$ , we apply a 80% to 20% training-validation split of the over-expression samples. If  $n_j < 100$ , we would use all the samples in  $X_j$  for  $\mathcal{D}_{\text{train}}$  due to an insufficient number of training samples.

Furthermore, we apply the **log1p** transformation to prevent negative predictions of gene expression and mitigate length biases in expression counts (Gorin & Pachter, 2023). This transformation results in a substantial improvement in model performance.

### A.2. Model Specifications

PerturbODE utilizes adaptive Runge-Kutta of order 5 of Dormand-Prince-Shampine which provides an exceptionally high order of accuracy and leverages its adaptive step size for efficient ODE solving. The adaptive step size also detects and handles a wide range of stiff ODEs. Differentiable numerical solution is computed via the adjoint method implemented in PyTorch by Chen (2021), available at <https://github.com/rtqichen/torchdiffeq>. The Sinkhorn-based  $W_2$  distance is differentiable through the *GeomLoss* implementation in PyTorch (Feydy et al., 2019).

For the baseline methods, the authors of DCDFG have implemented DCDI, DCDFG, NO-TEARS, and NO-TEARS-LR in the repository Lopez (2024), available at <https://github.com/Genentech/dcdfg>. Bicycle is implemented by Rohbeck et al. (2024) with code available at <https://github.com/PMBio/Bicycle>.

#### A.2.1. THRESHOLDS

We apply a threshold  $\epsilon$  to the GRN matrix  $\mathbf{G}$ , where any edge with a weight below  $\epsilon$  is set to 0 and any edge whose weight exceeds  $\epsilon$  is set to 1.

PerturbODE’s  $\epsilon$  threshold is determined using the formula  $\epsilon = c \cdot \sigma$ , where  $\sigma$  represents the standard deviation of the inferred GRN matrix  $\mathbf{G}$  across all entries, and  $c$  is a positive scalar. For SERGIO simulated data with 400 genes,  $c = 0.1$ , while for SERGIO simulated data with 100 genes and TF Atlas,  $c = 0.01$ .  $c$  is chosen so that the PerturbODE predicts a reasonable number of edges (no more than 30% of possible edges). A lower threshold is chosen for the clarity of presentation by getting similar number of edges as DCDI.

As recommended by their authors, DCDFG determines the threshold  $\epsilon$  through binary search, using depth of 20 evaluations of an exact acyclicity test to find the largest possible DAG for each method. NO-TEARS and NO-TEARS-LR’s  $\epsilon$  are chosen to be 0.3 while DCDI’s is set to 0.5 as recommended by the respective authors. For DCDI, NO-TEARS and NO-TEARS-LR different thresholdings such as binary search are attempted without meaningful change to the result. Different fixed values for  $\epsilon$  were also experimented for DCDFG without improvements. The author of Bicycle did not include disclose the appropriate threshold. We found the threshold of 0.005 to be the only one yielding reasonable results.

A.2.2. HYPERPARAMETERS

Spectral radius is used as the DAG constraint for DCDI, DCDFG, NO-TEARS, and NO-TEARS-LR. Notably, NO-TEARS and DCDI fail to run at dimensions higher than tens of variables with the trace exponential constraint. As recommended by the authors, we set the optimizer learning rate to 0.001 and the regularization coefficient to 0.1.

For Bicycle, the hyper-parameters are chosen as following: learning rate = 0.001, gradient\_clip\_var = 0.001, scale\_kl = 1, scale\_spectral = 0, and scale\_lyapunov = 0.1.

The number of modules is optimally set to 10 for NO-TEARS-LR and DCDFG. For PerturbODE, we set the number of modules to 100 for simulated data and 200 for TF Atlas. Details on performances across different number of modules in all models can be found in Figure 10.

As the number of modules increases, the model becomes closer to approximating the full graph. On the TF Atlas dataset, we demonstrate that the validation loss for PerturbODE decreases as the number of modules increases, plateauing after reaching 200 modules when training on TF Atlas (Fig. 7).

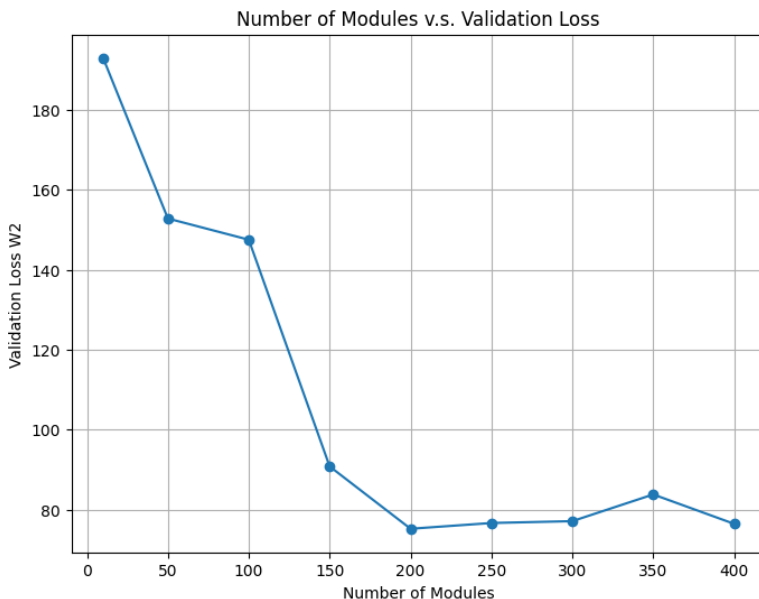


Figure 7. PerturbODE: number of modules v.s. validation loss in TF Atlas

On a separate note, PerturbODE uses 50 time steps for both diffused and non-diffused training when solving the ODE numerically. For diffused training, the time step duration  $t$  is set to 0.1, while for non-diffused training, it is set to 25. The lasso regularization coefficient,  $\lambda$ , is set to 0.001. When computing the  $W_2$  distance through Sinkhorn’s algorithm, the coefficient for entropic regularization is set to 0.05.  $\Delta t$  for the Brownian motion used to generate diffused data is set to 0.3.

A.3. Comparison to Erdős-Rényi Random Graphs

We generate 10,000 random graphs with the same density as our inferred GRN to numerically simulate the test statistics under Erdős-Rényi random matrices. The p-value is calculated using the equation,

$$p\text{-value} = \frac{1 + \#\{\tau^* \geq \tau\}}{1 + \Pi} \tag{6}$$

where  $\tau$  is the test statistic,  $\Pi$  indicates the total number of random graphs, and  $\tau^*$  denotes the test statistics computed from each graph. The p-value quantifies how often a test statistic is observed (or a more extreme one) purely by chance.

When evaluating SERGIO simulated data, the test statistics used is the F1 score, whereas recall score is used for TF Atlas

due to availability of only positive benchmark edges. To identify gene modules, we use test statistics based on the count of incoming edges to the module and outgoing edges from the module that are consistent with known regulatory relationships. Further, to identify the network motif of negative auto-regulation, test statistics is the number of negative self-loops.

#### A.4. Sampling from Linear SCMs for TF Atlas

For a learned GRN represented by  $\mathbf{W}$  (ensured to be a DAG, or thresholded to enforce acyclicity), we sample from linear structural causal models (SCMs) using the following procedure. First, for each parent gene  $i$  (master regulator) in the GRN, if not over-expressed, its expression level  $X_i$  is sampled from a normal distribution,  $X_i \sim \mathcal{N}(\mu, \sigma)$ , where  $\mu$  and  $\sigma$  represent the mean and standard deviation of gene expression levels across all genes and cells in the TF Atlas, respectively. If  $X_i$  is over-expressed, it is instead sampled from  $X_i \sim \mathcal{N}(\mu_\gamma, \sigma_\gamma)$  where  $\mu_\gamma$  and  $\sigma_\gamma$  are the mean and standard deviation of gene expression levels in over-expression genes across all over-expressed cells.

Downstream genes are realized in Equation 7:

$$\begin{aligned}
 X_i &= \sum_{X_j \in \text{pa}(X_i, \mathbf{W})} \mathbf{W}_{j,i} X_j && \text{if } X_i \text{ is not over-expressed,} \\
 X_i &= \sum_{X_j \in \text{pa}(X_i, \mathbf{W})} \mathbf{W}_{j,i} X_j + \gamma_i, \quad \gamma_i \sim \mathcal{N}(\mu_\gamma - \mu, \sigma_{\Delta\gamma}) && \text{if } X_i \text{ is over-expressed,}
 \end{aligned}
 \tag{7}$$

where  $\sigma_{\Delta\gamma}$  is the standard deviation of the differences between over-expressed genes and mean expression levels (average over genes) across all over-expressed cells. Further,  $\text{pa}(X_i, \mathbf{W})$  denotes all the parent genes (regulators) of gene  $i$  in the GRN  $\mathbf{W}$ .

#### A.5. Additional Thresholded Result

PerturbODE demonstrates significantly higher precision, recall, and F1 scores compared to DCDFG, NO-TEARS, and NO-TEARS-LR, while performing comparably to DCDI in these metrics (Fig. 9, Fig. 8). DCDI is the state-of-the-art method that outperforms PerturbODE in lower dimensional simulated datasets (100 – 400 genes), but it lacks scalability. In fact, for dimensions greater than 400, DCDI simply fails to execute, even with the more computationally feasible spectral radius acyclicity constraint. Details of the performance across all models with varying numbers of modules are provided in A.5.2. PerturbODE’s main contribution is its ability to train on real datasets with thousands of genes, while maintaining competitive predicative performance.

For evaluation, we threshold the weights of the output GRNs to obtain classification metrics (details in Appendix A.2.1). To further address the discrepancies between graph sparsity and predictive performance, we employed random graphs to generate an empirical null for each test statistic for random graphs with the same edge density. We compare the precision-recall test statistics of the predicted GRN against those from 10,000 Erdős-Rényi random networks, yielding empirical  $p$ -values (for details, see Appendix A.3). It is important to note that we were not able to find any threshold for Bicycle, where the model predicts significantly better than random ( $p$ -value  $\leq 0.1$ ).

There is considerable variation in recall scores for PerturbODE especially in the simulated yeast dataset. This is likely due to the high sparsity in the ground truth GRN, which leads to weak signals in the simulated dataset. This results in false negatives. Further,  $L_1$  penalty is enforced on the individual matrix. As multiplication of sparse matrices is not always sparse, the number of predicted edges tend to fluctuate. Denser predictions would have higher recall scores.

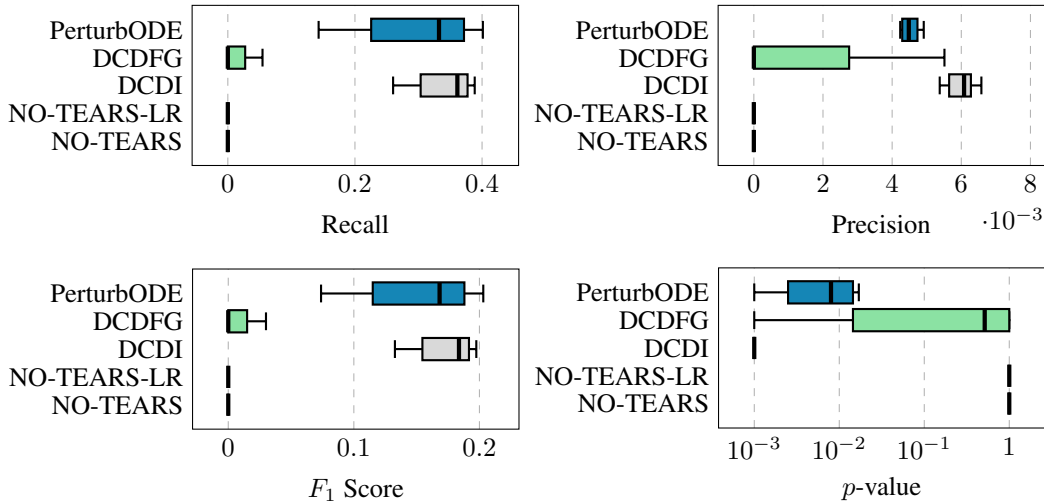


Figure 8. Performance metrics on SERGIO-simulated data of a known yeast GRN (400 genes), assuming perfect intervention over-expression (CRISPR-a).

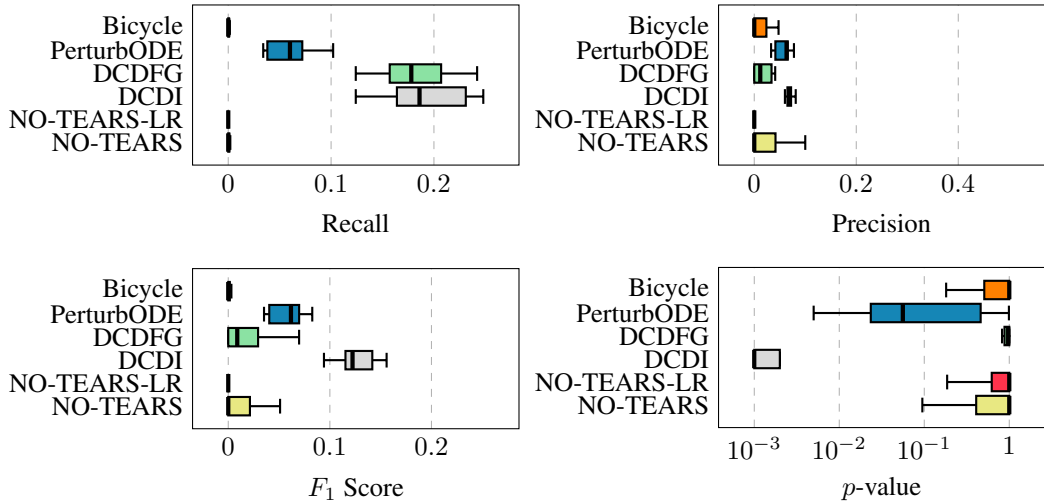


Figure 9. Performance metrics on SERGIO-simulated data of 10 random acyclic GRNs (100 genes), assuming perfect intervention over-expression (CRISPR-a).

#### A.5.1. NUMBER OF EDGES PREDICTED

Table 3 presents the number of edges predicted by each model across different datasets using the recommended thresholds. NO-TEARS and NO-TEARS-LR often under-predict, frequently resulting in near-empty graphs. While PerturbODE tends to over-predict, its  $p$ -values in comparison to random Erdős-Rényi matrices remain statistically significant. Similarly, DCDFG and DCDI also over-predict, though to a lesser extent compared to PerturbODE. For simulated data, AUPRC (Figure 8, 9) is the more appropriate metric in evaluation of model performances.

Table 3. Average number of edges predicted by all methods across datasets

METHOD	GROUND TRUTH	PERTURBODE	NO-TEARS	NO-TEARS-LR	DCDI	DCDFG
YEAST GRN ( $dim = 400$ )	623	43655.0	0.0	0.0	24332.8	4293.8
RANDOM DAGs ( $dim = 100$ )	500	552.0	0.0	7.1	1423.7	215.1
TF ATLAS ( $dim = 817$ )	N/A	101404.2	438.0	76.0	N/A	72884.0

A.5.2. GRN INFERENCE RESULTS WITH DIFFERENT NUMBER OF MODULES

PerturbODE and NO-TEARS-LR maintain consistent performance across different numbers of modules, while DCDFG achieves its best results with 10 modules. Figures 10 and 11 illustrate the performance of all models across varying number of modules in the SERGIO and TF Atlas datasets.

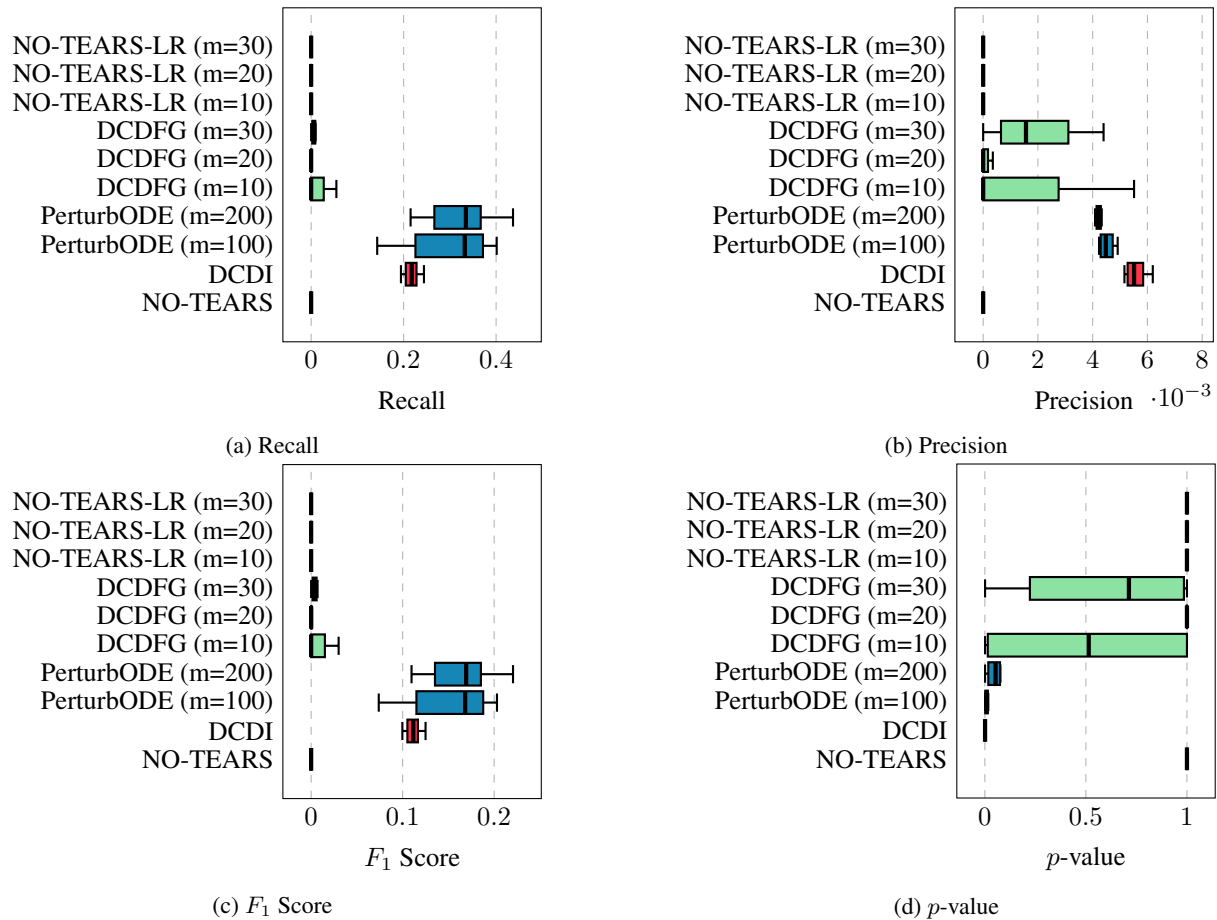


Figure 10. Perfect intervention over-expression (CRISPR-a) SERGIO simulation GRN inference. Ground truth GRN is a known yeast GRN (400 genes). Models with different number of modules are compared.

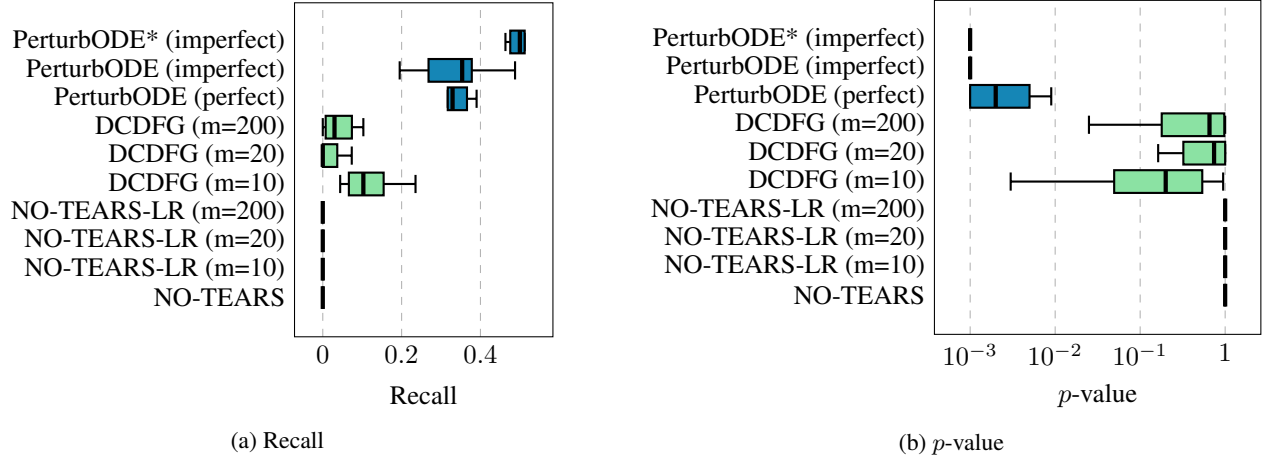


Figure 11. GRN Inference on TF Atlas Dataset (817 genes). Models with different numbers of modules are compared.

**A.6. Additional Results**

**A.6.1. MEAN AND STANDARD DEVIATION OF RESULTS**

Method	Recall		Precision		AUPRC		F1		p-value	
	Mean	Std	Mean	Std	Mean	Std	Mean	Std	Mean	Std
PerturbODE	0.3191	0.0937	0.0046	0.0003	0.0044	0.0002	0.1618	0.0468	0.0212	0.0260
DCDFG	0.0315	0.0414	0.0026	0.0032	0.0041	0.0003	0.0170	0.0223	0.6058	0.4829
NO-TEARS-lr	0.0000	0.0000	0.0000	0.0000	0.0027	0.0015	0.0000	0.0000	1.0000	0.0000
NO-TEARS	0.0000	0.0000	0.0000	0.0000	0.0019	0.0000	0.0000	0.0000	1.0000	0.0000
DCDI	0.3499	0.0470	0.0061	0.0004	0.0059	0.0001	0.1780	0.0237	0.0010	0.0000

Table 4. Mean and standard deviation across models for yeast simulated by SERGIO

Method	Recall		Precision		AUPRC		F1		p-value	
	Mean	Std	Mean	Std	Mean	Std	Mean	Std	Mean	Std
DCDI	0.3499	0.0470	0.0061	0.0004	0.0059	0.0001	0.1780	0.0237	0.0010	0.0000
NO-TEARS-lr	0.0000	0.0000	0.0000	0.0000	0.0027	0.0015	0.0000	0.0000	1.0000	0.0000
DCDFG	0.0315	0.0414	0.0026	0.0032	0.0041	0.0003	0.0170	0.0223	0.6058	0.4829
PerturbODE	0.3191	0.0937	0.0046	0.0003	0.0044	0.0002	0.1618	0.0468	0.0212	0.0260
NO-TEARS	0.0000	0.0000	0.0000	0.0000	0.0019	0.0000	0.0000	0.0000	1.0000	0.0000

Table 5. Mean and standard deviation across models for random DAGs simulated by SERGIO

Method	Recall		p-value	
	Mean	Std	Mean	Std
NO-TEARS	0.0000	0.0000	1.0000	0.0000
NO-TEARS-lr	0.0000	0.0000	1.0000	0.0000
DCDFG	0.1353	0.0692	0.4158	0.3692
PerturbODE (imperfect interv)	0.3659	0.0556	0.0042	0.0032
PerturbODE* (imperfect interv)	0.4976	0.0195	0.0010	0.0000
PerturbODE (perfect interv)	0.3561	0.0946	0.0236	0.0452

Table 6. Mean and standard deviation across models for TF Atlas

A.6.2. PREDICTION ON UNSEEN INTERVENTIONS (INDIVIDUAL TFs)

TF Over-expression	PerturbODE	NO-TEARS-LR	NO-TEARS
ZNF69	85.3758	106.0157	164.8816
SETDB1	261.9399	97.1853	157.8617
POU2AF1	300.8073	105.4930	163.0949
ZBTB37	69.4434	107.1228	165.9257
IRF3	73.6372	111.1662	170.1261
ID1	79.6410	109.7050	168.6616
TEAD1	244.5535	106.0757	163.4510
ASCL1	94.0845	134.7678	192.7295
KCNIP4	82.6612	104.7195	163.7381
MSX2	66.6919	103.6894	164.6299

Table 7. Test errors ( $W_2$ ) for TF over-expressions across different models.

A.7. Ablation Study & Power Analysis

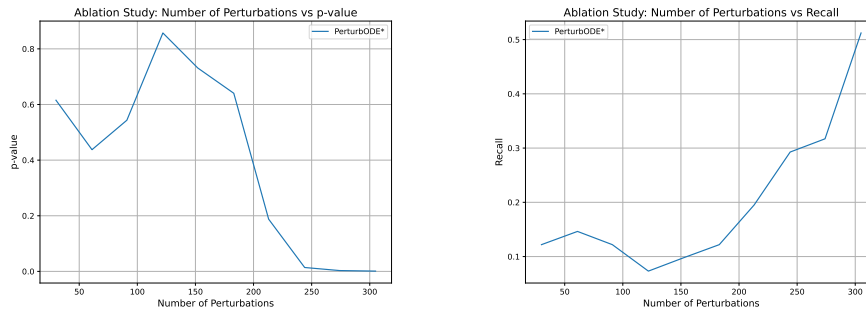


Figure 12. Ablation study: TF Atlas number of perturbations v.s. recall and p-value.

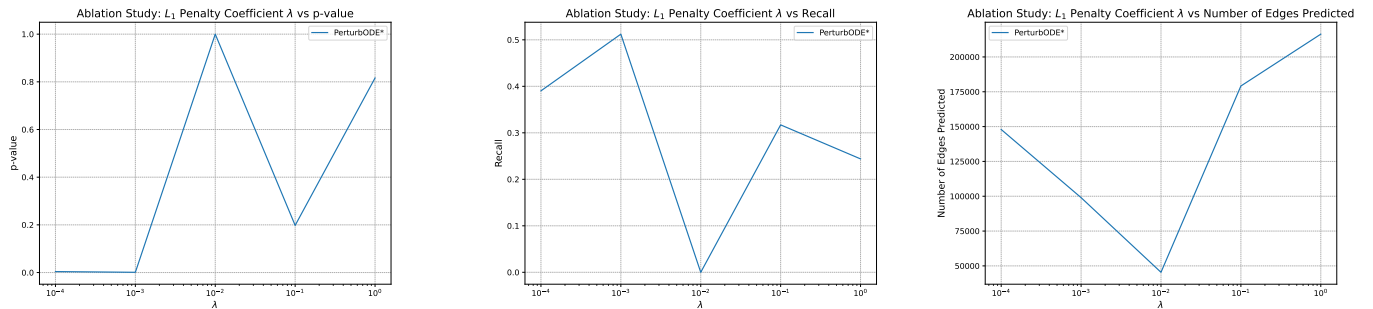


Figure 13. Ablation study: TF Atlas  $L_1$  penalty coefficient  $\lambda$  v.s. recall, p-value, and number of edges predicted.

Ablation study is done for PerturbODE\* trained on TF Atlas. Figure 12 shows the number of perturbations included for training plotted against recall and p-value. It is clear that as the number of perturbations grow, recall increases and p-value decreases. Figure 13 shows the change in recall and p-value when varying the  $L_1$  penalty coefficient for  $B$ . Ablation study shows that PerturbODE\* yields statistically significant result when  $\lambda \leq 0.001$ . Further, it is evident that as  $\lambda$  increases above 0.01, the number of edges predicted increase again. Our GRN is encoded as  $G = A \text{diag}(\alpha)B$ . The multiplication of sparse matrices is not necessarily sparse. Further analysis shows strong penalization of  $B$  leads to overly dense  $A$ , as the model resorts to  $A$  for data fitting. This could lead to a rise of the number of edges predicted.

A.7.1. PREDICTION ON UNSEEN INTERVENTION ALL UMAP AND PCA PLOTS

Figures 14, 14, show the detailed results on prediction on test data (unseen intervention) through UMAP and PCA.

# Interpretable Neural ODEs for Gene Regulatory Network Discovery under Perturbations

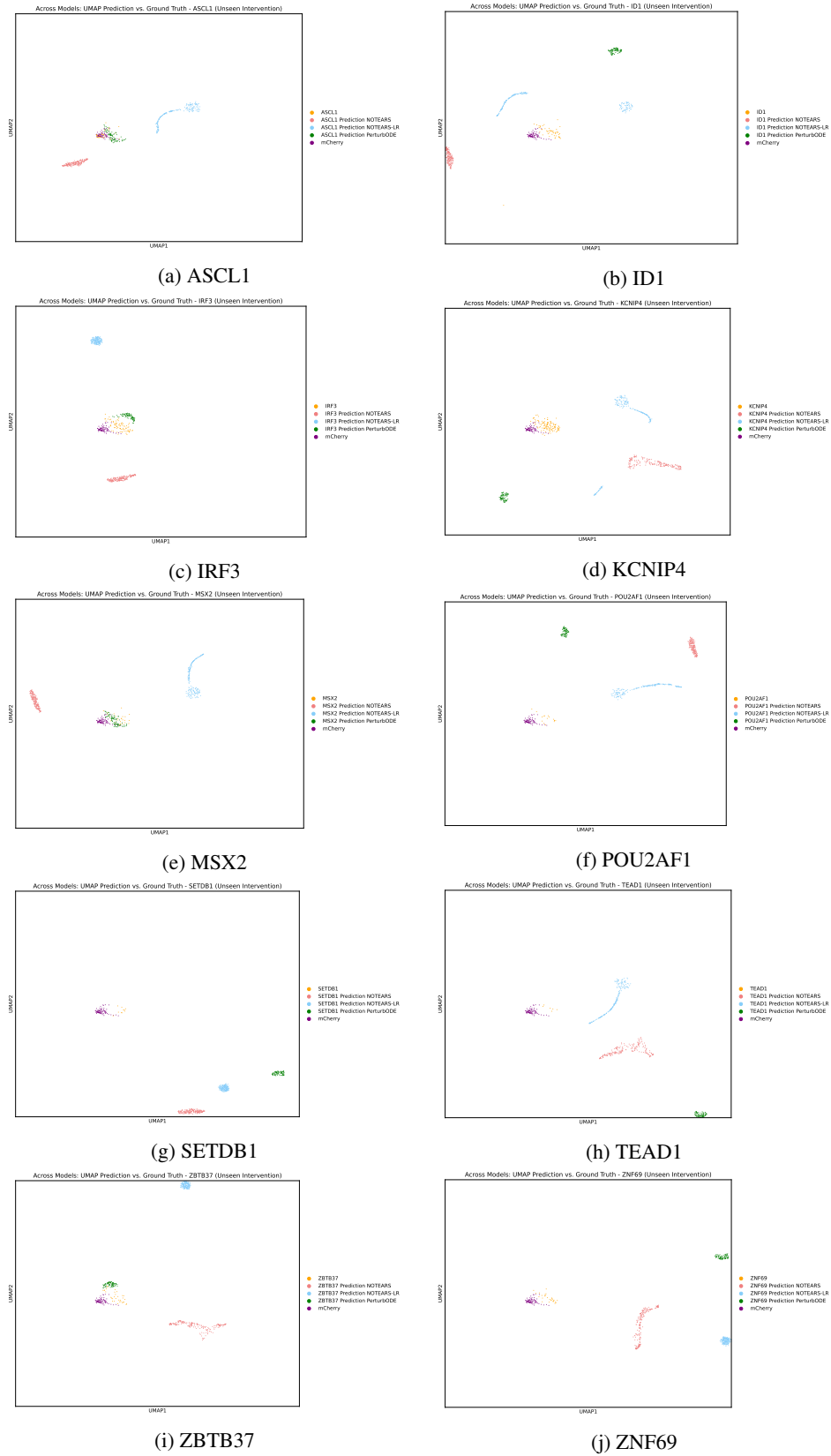


Figure 14. UMAP of predictions on unseen interventions across models.

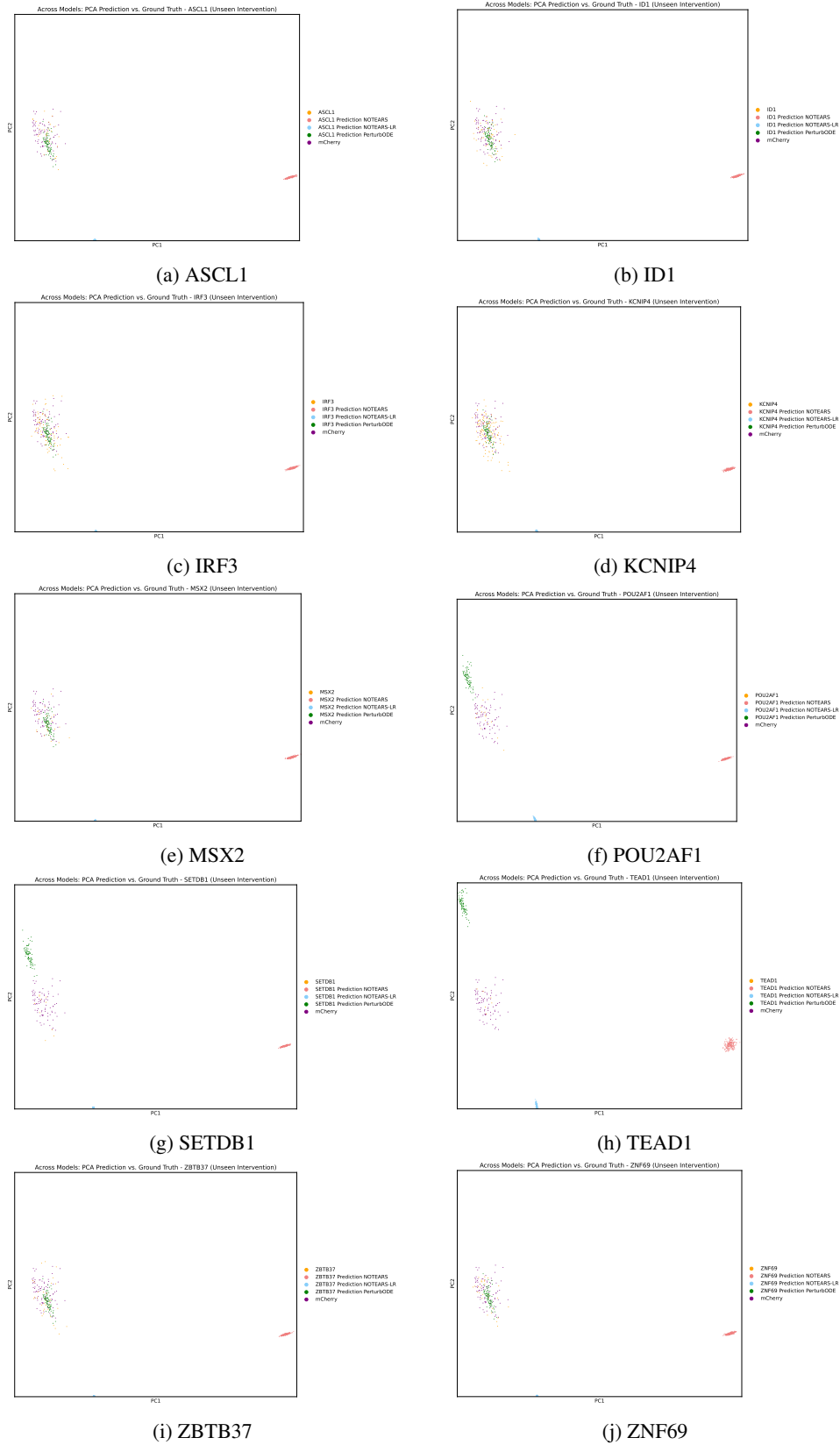


Figure 15. PCA of predictions on unseen interventions across models.

### A.8. PerturbODE Model Training

After training, the average  $W_2$  distance on both the training and held-out validation datasets decreases significantly and converges. The convergence rate of the  $W_2$  distance varies for each TF in the training and validation sets.

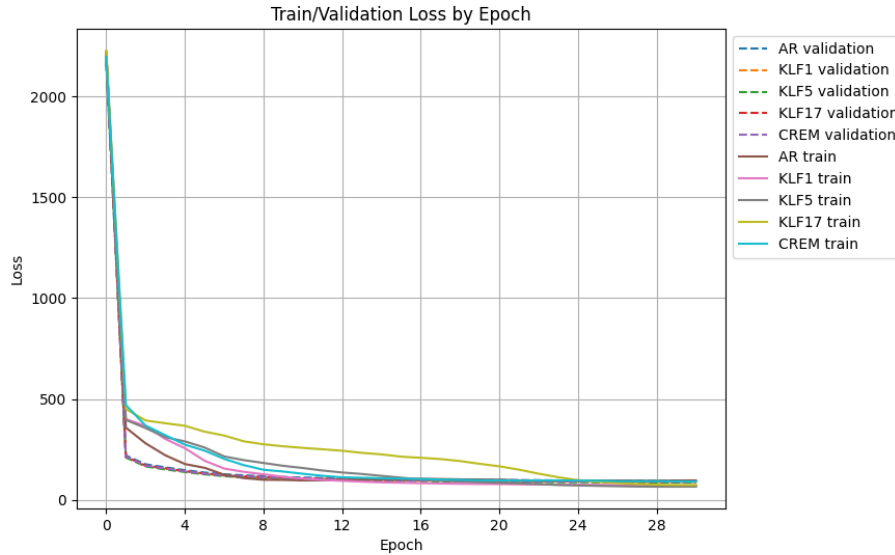


Figure 16. Convergence of  $W_2$  losses for trajectory predictions of training and validation samples per TF. Average validation loss on TF Atlas is 78.88.

### A.9. Ground truth GRNs from TF Atlas

The three GRNs with high confidence inferred in [Joung et al. \(2023\)](#) are consistent with their induced cell types and roles in development. GRHL1 and GRHL3 target TFAP2C and the TEAD family of TFs to induce trophoblasts, while FLI1 targets AP-1 family TFs (such as JUN and FOS) and ETV2 to induce vascular endothelial cells ([Krendl et al., 2017](#); [Dejana et al., 2007](#)). The GRN consisting of CDX1, CDX2, and HOXD11-influences posterior HOX genes is known to contribute to the definition of the anterior-posterior axis ([Neijts et al., 2017](#)). The three GRNs are in Figures 17, 18, 19.

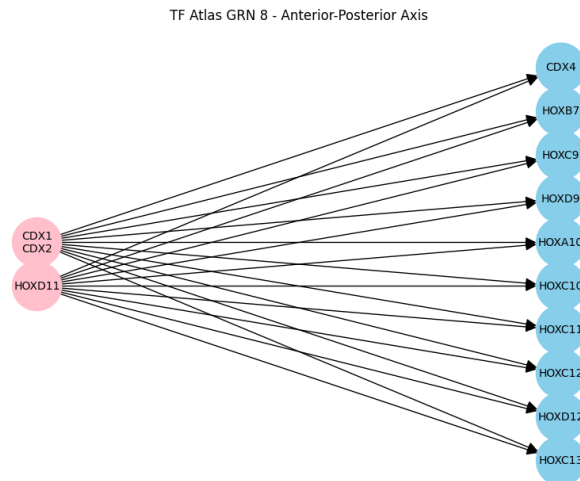


Figure 17. GRN with high confidence from TF Atlas - GRN8

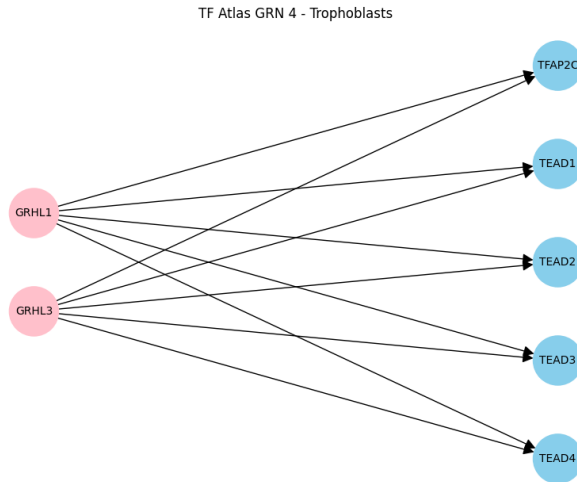


Figure 18. GRN with high confidence from TF Atlas - GRN4

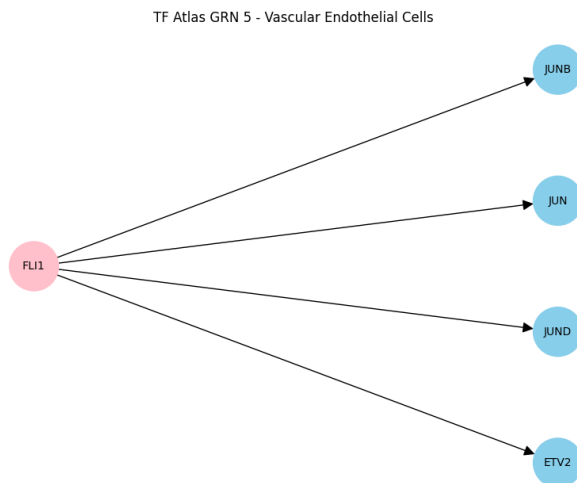
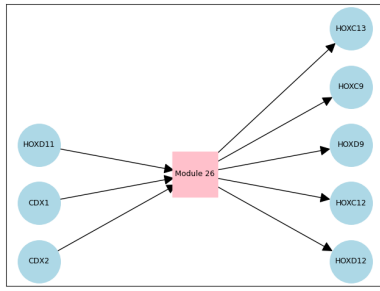
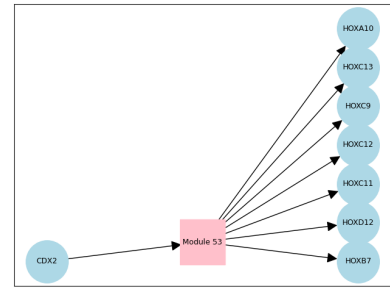


Figure 19. GRN with high confidence from TF Atlas - GRN5

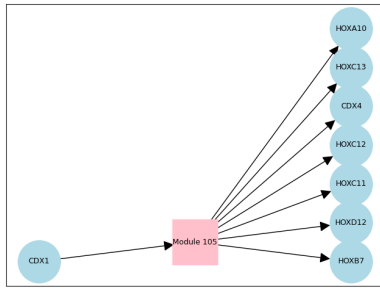
A.10. Inferred Modules Encapsulating Ground Truth GRNs



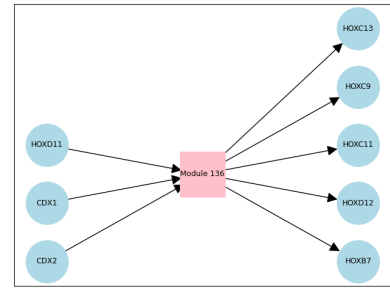
(a) Module 26



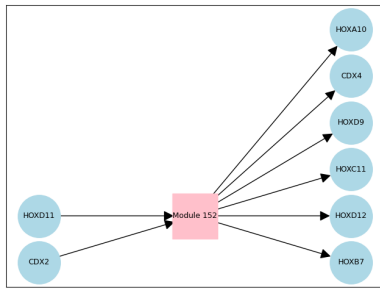
(b) Module 53



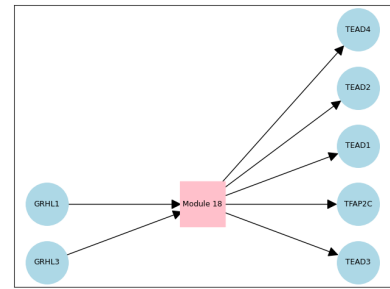
(c) Module 105



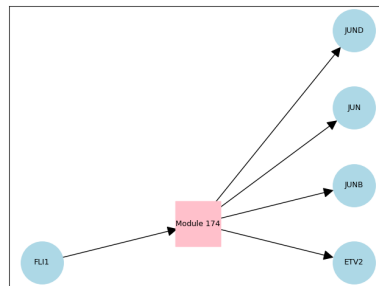
(d) Module 136



(e) Module 152



(f) Module 18



(g) Module 172

Figure 20. Modules identified by PerturbODE that align with established regulatory relationships.

A.11. SERGIO simulation

SERGIO proposes simulation of scRNA-seq data by sampling a directed acyclic GRN through a SDE (Dibaeinia & Sinha, 2020). Although SERGIO does not support interventional data, we modified its framework to simulate gene over-expression with perfect interventions (CRISPR-a). For each interventional regime  $I \in \mathcal{I}$ , the SDE is parameterized in the following

Equation 8.

$$dX_t = \left( M \left( P(X_t) - \lambda \circ X_t \right) + \sum_{j \in I} \gamma_j \cdot \delta_j \right) dt + q \circ \left( \sqrt{P(X_t)} dW_\alpha + \sqrt{\lambda X_t} dW_\beta \right) \quad (8)$$

The infinitesimal change of expression level (which is the stochastic process  $X_t$ ) of gene  $j$  at time  $t$  over an infinitesimal time interval  $dt$ , denoted as  $(dX_t)_j$ , is governed by its production rate  $P_j(X_t)$ , which is modulated by its regulators according to a given GRN in Equation 9. It also depends on the decay rate  $\lambda \in \mathbb{R}_+^d$  and the noise amplitude  $q \in \mathbb{R}^d$  influencing its transcriptional variability.  $M$  and  $\sum_{j \in I} \gamma_j \cdot \delta_j$  are the masking matrix and the over-expression term analogous to those in Equations 1 and 2.

$$P_j(X) = \sum_{j=0}^d p_{ji}(X) + b_j \quad \text{for } p_{ji} \text{ in 10, 11} \quad (9)$$

$$p_{ji}(X) = K_{ji} \frac{X_i}{h + X_i} \quad \text{if regulator } i \text{ is an activator of gene } j \quad (10)$$

$$p_{ji}(X) = K_{ji} \left( 1 - \frac{X_i}{h + X_i} \right) \quad \text{if regulator } i \text{ is a repressor of gene } j \quad (11)$$

For each pair of genes  $i$  and  $j$ , the coefficients are initialized as in 12.

$$\begin{aligned} \lambda_j &\sim \mathcal{N}(0.8, 0.2)_+ \quad , \quad K_{ji} \sim \mathcal{U}(0, 5) \quad , \quad q_j \sim \mathcal{U}(0.3, 1) \quad , \quad \gamma_j \sim \mathcal{N}(10, 1)_+ \quad , \\ h &= \frac{1}{d} \sum_{j=0}^d \frac{b_j}{q_j} \quad , \\ b_j &\sim \mathcal{N}(10, 0.01)_+ \quad \text{if gene } j \text{ is a master regulator,} \\ b_j &= 0 \quad \text{if gene } j \text{ is not a master regulator.} \end{aligned} \quad (12)$$

$W_\alpha, W_\beta \in \mathbb{R}^d$  are two independent Wiener processes. We numerically simulate the SDE in Equation 8 using the Euler-Maruyama Scheme (E et al., 2019) with  $\Delta t = 2$  in 50 steps.

$$\begin{aligned} (X_j)_{t+\Delta t} &= (X_j)_t + \left( \left( P_j(X_t) - \lambda_j X_j(t) \right) \cdot \mathbb{I}_{j \notin I} + \gamma_j \cdot \mathbb{I}_{j \in I} \right) \Delta t \\ &\quad + q_j \sqrt{P_j(X_t)} \Delta W_\alpha + q_j \sqrt{\lambda_j X_j(t)} \Delta W_\beta \end{aligned} \quad (13)$$

$$(\Delta W_\alpha)_j \sim \sqrt{\Delta t} \mathcal{N}(0, 1), \quad (\Delta W_\beta)_j \sim \sqrt{\Delta t} \mathcal{N}(0, 1) \quad (14)$$

Lastly, the SDE 8 is initialized at the expected fixed point  $X_0$  (where the drift of the SDE vanishes) with over-expression but without masking (perfect intervention). SERGIO assumes Jansen's Equality  $E[p_{ji}(X_i)] \approx p_{ji}(E[X_i])$  for simplicity of initialization (Dibaeinia & Sinha, 2020). Hence,  $X_0$  is initialized to the following expectations in Equations 15 and 16:

$$E[X_j] = \frac{\sum_{i=0}^d p_{ji}(E[X_i])}{\lambda_j} + \gamma_j \cdot \mathbb{I}_{j \in I} \quad \text{if } j \text{ is not a master regulator} \quad (15)$$

$$E[X_j] = \frac{b_j}{\lambda_j} + \gamma_j \cdot \mathbb{I}_{j \in I} \quad \text{if gene } j \text{ is a master regulator} \quad (16)$$

When simulating data using SERGIO, we use a real yeast GRN ( $dim = 400$ ) and 10 random DAGs ( $dim = 100$ ) with 500 binary entries (1 or 0). For clarity of comparison across models, the real yeast GRN is pruned to enforce acyclicity and include only positive directed edges. For both scenarios, the synthetic dataset generated by SERGIO includes 10,100 cells, created from 100 intervention schemes, each targeting 5 genes, along with one non-intervention scheme. Each regime provides 100 observations.

**A.12. Gene Module Example: Flagella of E. coli**

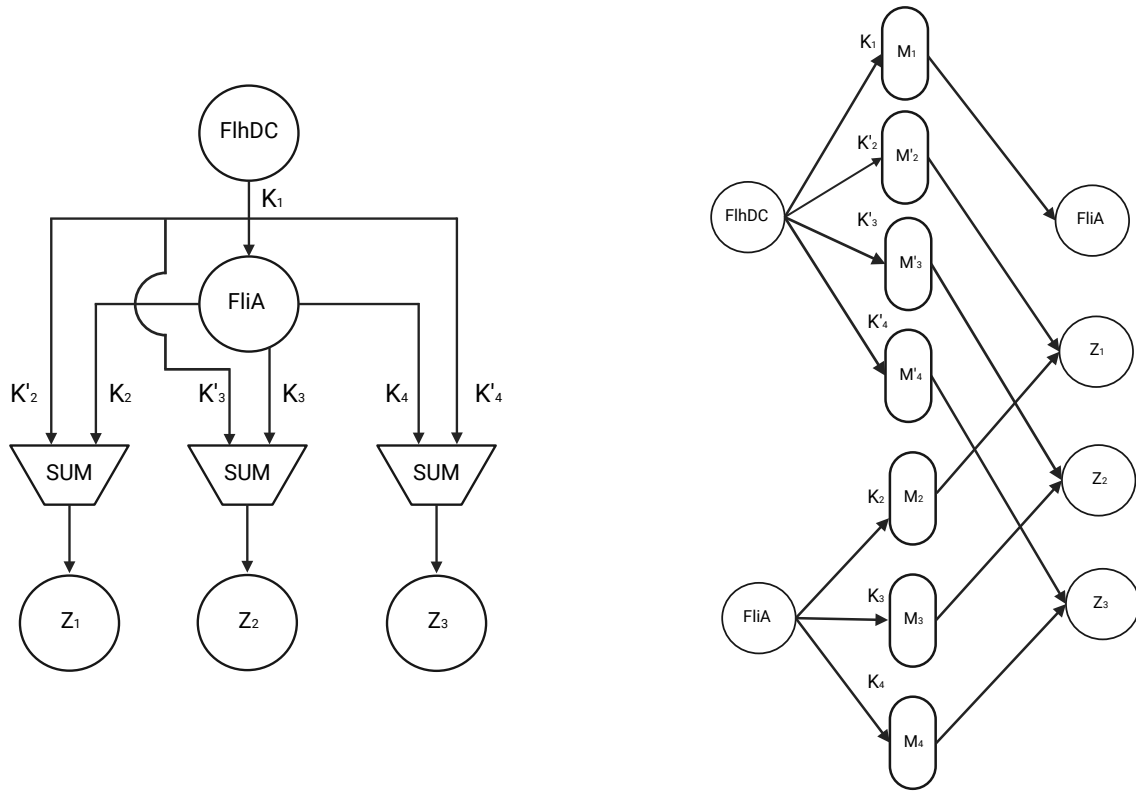


Figure 21. Regulatory circuit for the production of flagella in E. coli.

It is well established that the regulatory circuit responsible for the production of E. coli flagella follows the network motif of multiple-output Feedforward Loop (Alon, 2006, pp. 64-68). Its circuit is shown on the left of Figure 21, where FlhDC and FliA regulate  $Z_1, Z_2,$  and  $Z_3$ , which are operons encoding the proteins that make up the flagella of E. coli. (In fact, there are in total 6 operons for this process.) Each operon consists of a group of genes, and it is regulated by a weighted sum of non-linearly activated signals from FlhDC and FliA through Hill functions.

The order in which the operons are activated matches the order of proteins needed to assemble the flagella. The timing of activation is achieved by different activation thresholds in the Hill functions. If  $Z_1$  is activated before  $Z_2$ , which is activated before  $Z_3$ , then  $K_2 < K_3 < K_4$ . In other words,  $Z_1$  needs a lower concentration of FliA to be switched on. For example,  $Z_1$  would include the group of genes encoding the proteins for MS ring (base of flagella) and  $Z_3$  would be for the filament (tail of flagella). In PerturbODE, the activation threshold is tuned by the bias term,  $\beta$ , to the hidden neurons.

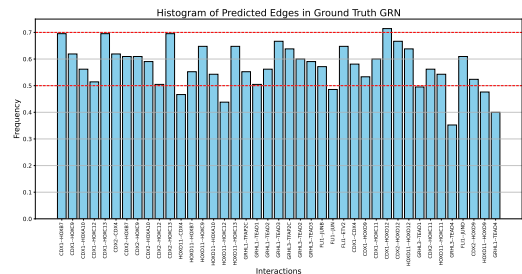
This structure can be represented in a two-layer MLP shown on the right of Figure 21. Each operon  $Z_i$  is regulated by the weighted sum of signals from two modules  $M_i$  and  $M'_i$ . The signals from FliA and FlhDC are first activated by Hill

functions with different activation thresholds before being transferred to modules  $M_i$  and  $M'_i$  respectively.

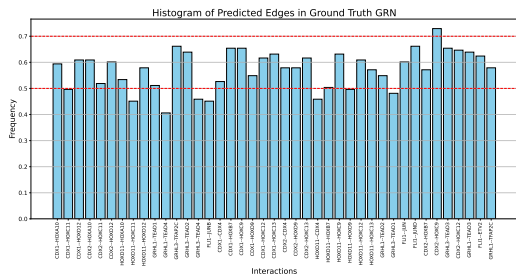
To represent this gene regulatory circuit with an adjacency matrix  $\mathbf{G} = A \text{diag}(\alpha)B$ , we multiply the two coefficient weight matrices of the MLP with an additional scaling to account for the rate of activation controlled by  $\alpha$ .

### A.13. Statistical Inference: Generalizability and Stability Analysis

For stability analysis, we bootstrapped (sampled with replacement) TF Atlas dataset 105 times to evaluate consistency in the edges selected by PerturbODE. We also filtered the list of TFs perturbations that PerturbODE trains on down to the TFs pertinent to the ground truth GRNs in order to reduce training time. Then the gene expression space is the union between the filtered TF list and the top 50 highly variable genes, resulting in 52 genes. For generalizability analysis, we performed a similar procedure but using 133 different train-validation split. Train-validation split is chosen to be 8-2, where, for each interventional distribution, 20% of samples are withheld for the validation set. The validation set is used as stopping criterion (a hyper-parameter) for training.



(a) Stability Analysis: Ground Truth Edges Selected by PerturbODE.



(b) Generalizability Analysis: Ground Truth Edges Selected by PerturbODE.

Figure 22. Comparison of Stability and Generalizability Analyses for Ground Truth Edges Selected by PerturbODE.

Figures 22a and 22b indicate that PerturbODE selects the ground truth edges roughly 50% to 70% of the time in both the stability and generalizability analyses. While a highly consistent model would ideally surpass a 75% selection rate, these results nonetheless reflect a reasonable degree of reliability given the inherent complexity of the task. Future enhancements to the model may further improve this consistency.

### A.14. Gene Enrichment Analysis

We performed gene enrichment analysis using the Reactome Pathway Database (2022) and the Gene Ontology Biological Process (2021) with hypergeometric test. The examined pathways were filtered to those relevant to the anterior-posterior axis and vascular endothelial cells. The upstream genes and downstream genes of each module are selected by taking those edges whose weights are greater than 2 standard deviations of  $B$  and  $A$  respectively. Figure 25 illustrates the clustering of modules based on specific functions. A significant number of modules exhibit enrichment for anterior-posterior specification—a pathway crucial in development. This observation is expected, considering that the TF Atlas comprises human embryonic stem cells.

To show that the modules are not selecting identical genes, we plotted histograms of genes selected by various modules. Figure 23 shows a histogram of genes selected by the highlighted modules we selected for evaluation in Section 4.2.1, and Figure 24 showcases that of 10 randomly selected modules. Both histograms show clear clustering of gene selections by modules.

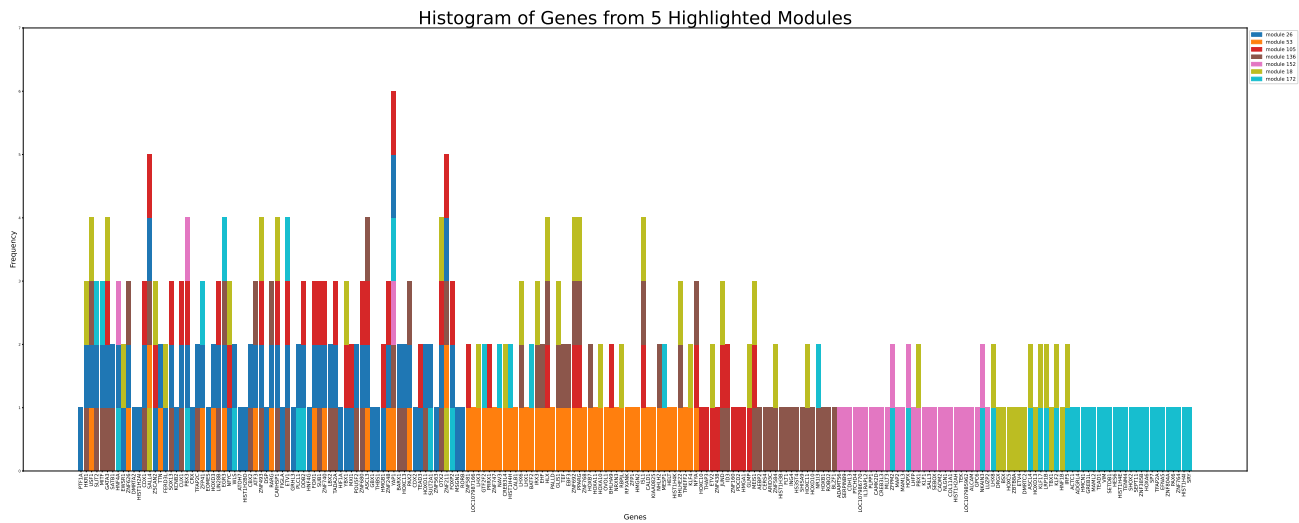


Figure 23. Histogram of Genes from 5 Highlighted Modules.

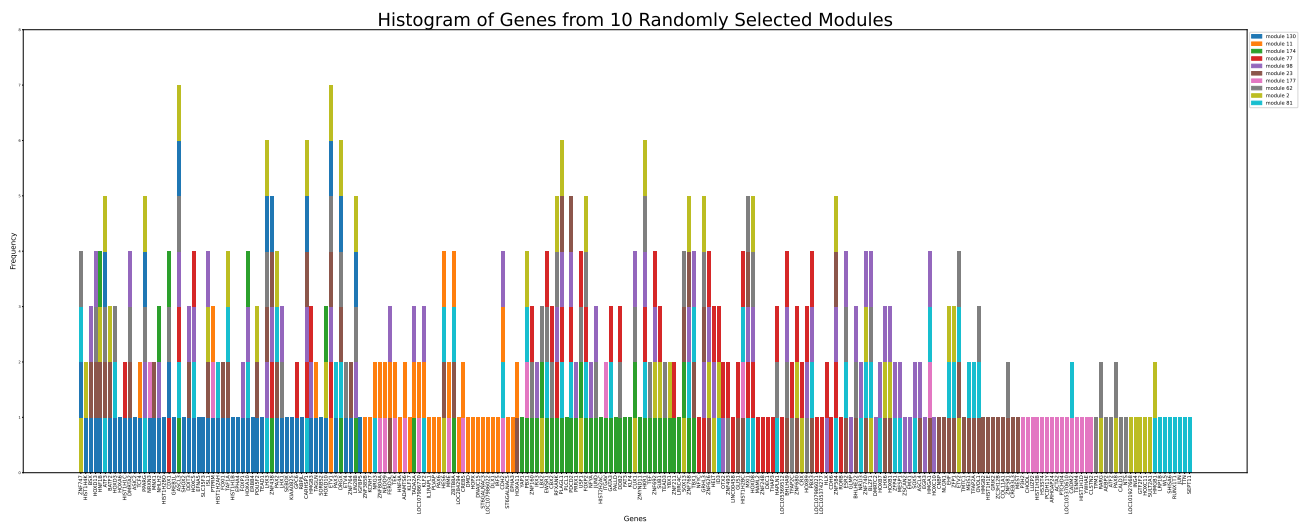


Figure 24. Histogram of Genes from 10 Randomly Selected Modules.

